

<https://doi.org/10.1038/s44310-025-00060-x>

# Linear optical wave energy redistribution methods for photonic signal processing



Connor Rowe<sup>1</sup>, Xinyi Zhu<sup>1</sup>, Benjamin Crockett<sup>1</sup>, Geunweon Lim<sup>1</sup>, Majid Goodarzi<sup>1</sup>, Manuel Fernández<sup>2</sup>, James van Howe<sup>3</sup>, Hao Sun<sup>1</sup>, Saket Kaushal<sup>1</sup>, Afsaneh Shoeib<sup>1</sup> & José Azaña<sup>1</sup>✉

Manipulating the phase of an optical wave over time and frequency gives full control to the user to implement a wide variety of energy preserving transformations directly in the analogue optical domain. These can be achieved using widely available linear mechanisms, such as temporal phase modulation and spectral phase filtering. The techniques based on these linear optical wave energy redistribution (OWER) methods are inherently energy efficient and have significant speed and bandwidth advantages over digital signal processing. We describe several recent OWER methods for optical signal processing, including denoising passive amplification, real-time spectrogram analysis, passive logic computing, and more. These functionalities are relevant whenever the signal is found on a classical or quantum optical wave, or could be upconverted from radio frequencies or microwaves, and they are of interest for a wide range of applications in telecommunications, sensing, metrology, biomedical imaging, and astronomy. The energy preservation of these methods makes them particularly interesting for quantum optics applications. Furthermore, many of the individual components have been demonstrated on-chip, enabling miniaturization for applications where size and weight are a main constraint.

The transition from electrical to optical technologies for the transmission of information is what enabled the Internet as we know it today<sup>1</sup>. The extraordinary pace of improvements in bandwidth, speed, energy efficiency, and cost of optical fibres provided the foundation for the revolutionary growth of available information over the past three decades. Alongside the developments of optical technologies for transmitting information, the increased demand for higher information processing capabilities has been met by advances in digital signal processing (DSP). These technologies, based on electronic transistors, have so far kept pace in terms of number of components per unit area on a circuit, increased performance of those components, and cost under Moore's law and other scaling relations<sup>2–4</sup>. However, the physical size of transistors has reached the scale where quantum effects prevent their further miniaturization, and the difficulty of properly managing the heat generated from transistors at higher speeds limit their overall performance<sup>4,5</sup>. Therefore, researchers expect Moore's law to fail within the next decade<sup>3</sup>. These fundamental limitations have led naturally to the suggestion of replacing electronics with optics for the processing of information, just as how fiber optics replaced copper wires for data transmission in the 90s<sup>6</sup>. Some optical signal processing technologies already have a long history of application (see the history of optical amplifiers<sup>7</sup>, switches<sup>8</sup>, filters<sup>9</sup>,

and demultiplexers<sup>9</sup>). More advanced techniques await to provide the increased bandwidth, speed, energy efficiency, size, and cost reductions that will define the progress in the upcoming decades<sup>10</sup>.

In this review, we discuss recent developments in optical signal processing, restricting our attention to those set of technologies which rely on linearly redistributing (i.e., reusing) the energy of a one-dimensional analogue optical wave, thereby providing maximum energy efficiency. We refer to these methods as linear optical wave energy redistribution (OWER) techniques. While information can be encoded on the many degrees of freedom of photons such as polarization, orbital angular momentum, or position (for free space and multimode fiber optics), we focus here on time and frequency for their unique versatility and scalability in terms of information processing capacity. The information encoded in the signal over these degrees of freedom could be artificially placed there or originate from a natural phenomenon under investigation. For instance, in optical telecommunications, the information to be transmitted is most commonly encoded in the changes of the intensity and/or phase of an optical carrier wave along the time domain<sup>1</sup>. Optical signal processing here thus refers to a set of mathematical transformations implemented directly in the analogue optical domain to perform a specific target function for encoding,

<sup>1</sup>Institut National de la Recherche Scientifique – Centre Énergie Matériaux et Télécommunications, 800 Rue de la Gauchetière, H5A 1K6 Montréal, QC, Canada.

<sup>2</sup>Instituto Balseiro (UNCuyo-CNEA) & CONICET, RN 8400 Bariloche, Argentina. <sup>3</sup>Augustana College, 639 38th Street, 61201 Rock Island, IL, USA.

✉e-mail: [jose.azana@inrs.ca](mailto:jose.azana@inrs.ca)

processing, or detecting the information on the time and/or frequency degree of freedom of an optical wave. It is important to note that this approach is interesting whenever the information of interest is encoded on an optical wave, not just for applications in telecommunications<sup>1</sup>. Take for example the emerging field of astrophotonics, describing a whole range of new astronomical capabilities enabled by the reduced losses, increased bandwidth, and on-chip integration of photonics<sup>11</sup>. Or consider the field of biomedicine, where photonics has quickly become an irreplaceable tool for in vivo imaging and diagnostics<sup>12,13</sup>. Other examples include sensing, metrology, imaging, and spectroscopy using light waves at both the classical and quantum levels<sup>14–16</sup>. The information may also be originally encoded in RF waves or microwaves, and then modulated onto an optical frequency. Up-conversion from microwave to optical frequencies is a strategy that has been shown to effectively facilitate both the transmission and processing of these signals, particularly when they are high speed, extend over a broad bandwidth, or are on a high frequency carrier<sup>10,17</sup>. This strategy, generally referred to as “microwave photonics”, forms the basis of radio-over-fibre communications and has proven useful for many other applications, such as for software-defined radar, or microwave and mm-wave sensing and imaging<sup>16–18</sup>.

The key advantages of implementing information processing in the optical domain, rather than with digital electronic components, are speed and bandwidth. However, this is often achieved at the cost of increased power consumption and a larger form factor. Focusing on linear optics over nonlinear optics minimizes the power consumption, and restricting further to optical transformations which only redistribute the energy of the wave (i.e., in contrast to intensity modulation or filtering) theoretically maximizes the energy efficiency<sup>19</sup>. This is the general strategy we refer to as OWER. Minimizing losses and optimizing energy efficiency is generally desired but it is a particularly relevant requirement for processing ultra-low intensity light distributions, such as optical quantum states<sup>20,21</sup>. Another key advantage of OWER methods is that they can be readily implemented using off the shelf low-loss fibre-optic components that are commercially available. Furthermore, many of these efficient fibre-optic technologies have already been demonstrated on silicon waveguides or “on-chip”<sup>22</sup>. This strongly suggests the potential for future integration and miniaturization of both classical and quantum OWER techniques. Figure 1 shows a summary of some of the important functionalities which are enabled by OWER methods and will be discussed in this article.

The means by which wave energy redistribution is carried out involves a combination of linear phase-only transformations. Phase shift can be implemented over the two domains of interest, i.e. time and frequency. For both domains, a device implementing a phase transformation can be

thought of as a black box which changes in optical path length from the perspective of the incoming signal. Importantly, as the optical path length through a device is what is being modified, the energy is rearranged but overall, the total energy input into the device will be near to equal the total energy output, after accounting for an amount of minimizable loss.

In Chapter 2, we review the basic mathematical definitions and implementations of the two fundamental linear wave processing mechanisms used for the realization of OWER techniques, namely, spectral phase filtering (SPF) and temporal phase modulation (TPM). Chapter 3 begins the investigation into OWER techniques with spectral analysis and Fourier transformations using a single dispersive element. This is followed by a discussion of two more advanced methods for real-time spectral analysis, and the potential applications enabled by these state-of-the-art techniques. Chapter 4 discusses passive amplification of optical waveforms, resulting in particularly interesting results such as the mitigation of incoherent noise for both narrow and broadband waveforms. Chapter 5 gives an overview of other possible functionalities not presented in detail but that have been developed for specific use cases. In Chapter 6, the transformations previously introduced are demonstrated to have analogues in the quantum regime of low intensity signals, and the conceptual differences with the quantum versions are highlighted. Chapter 7 presents some recent realizations of OWER transformations in integrated and on-chip formats, leading to the practical implementation of the previously discussed techniques in application. Finally, Chapter 8 concludes the review and gives some examples of further directions to be investigated.

## Theory and Technology Implementations

### Theory

There are two main linear mechanisms that can be used to manipulate the phase profile of a temporal optical wave, enabling the implementation of efficient OWER methods on a target signal. One is spectral phase filtering (SPF), in which the wave phase profile is linearly manipulated along the frequency domain, and the other, is temporal phase modulation (TPM), in which the wave phase profile is modulated along the time domain<sup>23</sup>. To illustrate these manipulations, we briefly recall that a temporal signal  $a(t)$  is related to its spectrum  $A(\omega)$  by the Fourier transform,

$$A(\omega) = |A(\omega)|e^{i\Phi_A(\omega)} = \mathcal{F}\{a(t)\} = \int_{-\infty}^{\infty} a(t)e^{-i\omega t} dt, \quad (2.1)$$

which can be thought of as decomposing a temporal signal into a linear combination of different single-frequency components. Each is characterized by an amplitude variation (magnitude of the single-frequency

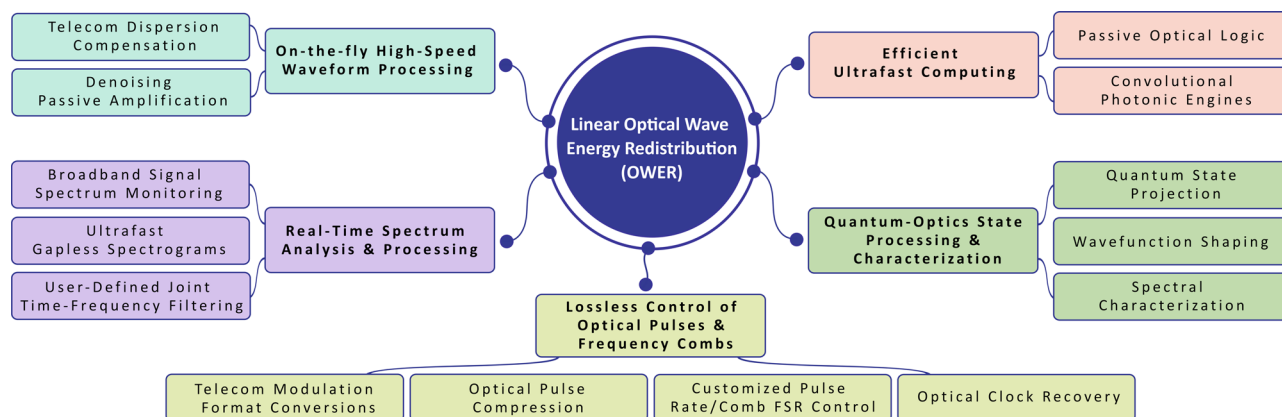
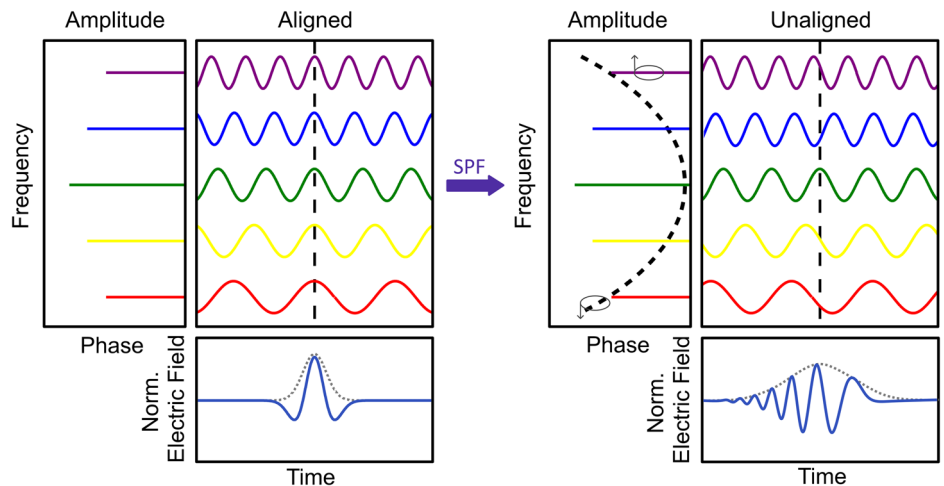


**Fig. 1 | Overview of key functionalities enabled by optical wave energy redistribution (OWER) techniques.** The fundamental basis of these functionalities are the two linear OWER techniques known as spectral phase filtering (SPF) and temporal phase modulation (TPM). Both simply rearrange the energy of an input optical wave to perform a desired mathematical transformation directly in the analogue optical domain. Chapter 3 deals with real-time spectral analysis and

processing functionalities. Chapter 4 treats on-the-fly high-speed waveform processing as well as lossless control of optical pulses and combs. Chapter 5 discusses other functionalities including optical logic and optical neural networks. Chapter 6 discusses extensions to and techniques unique to the quantum domain. Chapter 7 discusses how TPM and SPF at the heart of OWER methods can be implemented on chip.

**Fig. 2 | Depiction of spectral phase filtering (SPF) using second-order group-velocity dispersion (GVD).** This process demonstrates how each frequency component of an optical wave is independently manipulated along the frequency domain, following a quadratic phase shift profile shown as a dotted line over the frequency components. In this case, the example of an optical frequency comb is shown producing a short temporal pulse, whose envelope is shown with dotted lines. The result after the SPF process is a temporal broadening of the pulse shape, while the spectral intensities are not modified.



oscillation,  $|A(\omega)|$  and a phase delay  $\Phi_A(\omega)$  with respect to an overall time reference (e.g., zero time). The SPF and TPM are inherently linear mechanisms, as defined from a signal processing perspective<sup>24,25</sup>. In particular, we consider the system to be an operation  $H$ , in time or frequency, that we wish to implement on the signal. If  $H$  is a linear system, then

$$H\{\alpha a_1 + \beta a_2\} = \alpha H\{a_1\} + \beta H\{a_2\}, \quad (2.2)$$

for two inputs  $a_1$  and  $a_2$ , and two constants  $\alpha$  and  $\beta$ . We are particularly interested in the case where the system  $H$  is a multiplication with another function, as will be true for SPF systems (along the frequency domain) and TPM systems (along the time domain). In other words,

$$H\{a(s)\} = K(s)e^{i\Phi_H(s)} \cdot a(s), \quad (2.3)$$

over a domain variable  $s$  representing time or frequency, where  $K(s)$  and  $\Phi_H(s)$ , representing the magnitude and phase of the system  $H(s)$ , respectively, are not functions of the input  $a(s)$ . In this case, it is simple to show using the convolution theorem that the system is linear both in the time and frequency domains<sup>24</sup>. Equation (2.2) implies that impulses, or Dirac deltas, representing single frequency components in the spectral domain for SPF systems and localized amplitudes in the temporal domain for TPM systems, can be treated independently by the system and then the results combined. This means that for an SPF, each frequency component of a signal is transformed irrespective and independently of the rest. By knowing what the system does to each individual frequency, any combination can be reconstructed at the output. Furthermore, when considering phase-only operations such as SPF and TPM, we restrict ourselves to the operations where  $K(s) = 1$ , such that

$$|H\{a(s)\}|^2 = |e^{i\Phi_H(s)} \cdot a(s)|^2 = |a(s)|^2, \quad (2.4)$$

which implies that energy of the waveform, given by integrating Eq. (2.4), is not affected by the phase-only operation.

One of the ways to conceptualize how both the SPF and TPM mechanisms work is by considering the optical path length through an analogue device meant to implement such a transformation. SPF involves the implementation of a customized optical path length through the device depending on the frequency or wavelength of the optical wave. The different frequency components of the input signal are simply delayed with respect to each other following a prescribed phase shift profile<sup>24</sup>.

The relevant case of SPF that is inherent to a propagating optical electromagnetic (EM) wave in a dielectric material, such as a waveguide or an optical fibre, is chromatic dispersion. Mathematically, the relative

spectral phase shift  $\phi(\omega)$  can be expanded as a Taylor series,

$$H(\omega) = e^{-i\phi(\omega)} = \exp\left\{-i\phi_0 - i\dot{\phi}_0\omega' - i\frac{\ddot{\phi}_0}{2}\omega'^2 - \dots\right\}, \quad (2.5)$$

expanded around the wave's centre frequency  $\omega_0$  (carrier frequency). In this equation,  $\omega' = \omega - \omega_0$  defines the baseband frequency variable,  $\phi_0 = \phi(\omega_0)$  denotes the phase shift of the carrier frequency component,  $\dot{\phi}_0 = \frac{\partial\phi(\omega_0)}{\partial\omega}$  is the average group delay of the propagating wave, and  $\ddot{\phi}_0 = \frac{\partial^2\phi(\omega_0)}{\partial\omega^2}$  is referred to as group-velocity dispersion (GVD), also known as the second-order dispersion coefficient<sup>23,26</sup>. Assuming the bandwidth or range of frequencies is sufficiently narrow, all higher-order terms can be neglected. Often it is required to take the third-order dispersion term for example, when treating high speed telecommunications signals. GVD represents a linear group delay over frequency and can be positive, corresponding to a normal dispersion process, or negative, corresponding to an anomalous dispersion process. Focusing solely on the effect of GVD, the transfer function can be expressed as,

$$H(\omega) = e^{-i\phi(\omega)} = e^{-i\frac{\ddot{\phi}_0}{2}\omega'^2} \quad (2.6)$$

As mentioned above, Fig. 2 shows an illustration of the SPF process induced by a GVD medium on an incoming pulsed waveform. The different frequency components of the waveform are phase shifted with respect to one another following the expected quadratic phase profile, broadening the input pulse shape in time.

TPM also involves the implementation of a customized optical path length through a device, but depends on time instead of frequency. Figure 3 illustrates the special case of a time lens, the temporal analogue of a spatial thin lens<sup>27</sup>, detailed further below. It is convenient to think of the TPM device as slowly varying in length depending on time. The result is a change in the required number of optical cycles to traverse the device, modifying the phase of the cycle upon exit as a function of time. Mathematically, a TPM implemented in the temporal domain of a wave can be expressed as<sup>24</sup>,

$$H(t) = e^{i\varphi(t)}, \quad (2.7)$$

where  $\varphi(t)$  defines the relative phase shift introduced by the TPM process depending on time  $t$ . In practice, the optical path length of the device varies with time much slower than the optical carrier frequency, so that the phase modulation happens over many optical cycles.

For an indicative example, the specific TPM known as a time lens will be introduced. As a thin spatial lens provides a quadratic phase modulation depending on the transverse spatial variable<sup>28</sup>, a time lens provides a

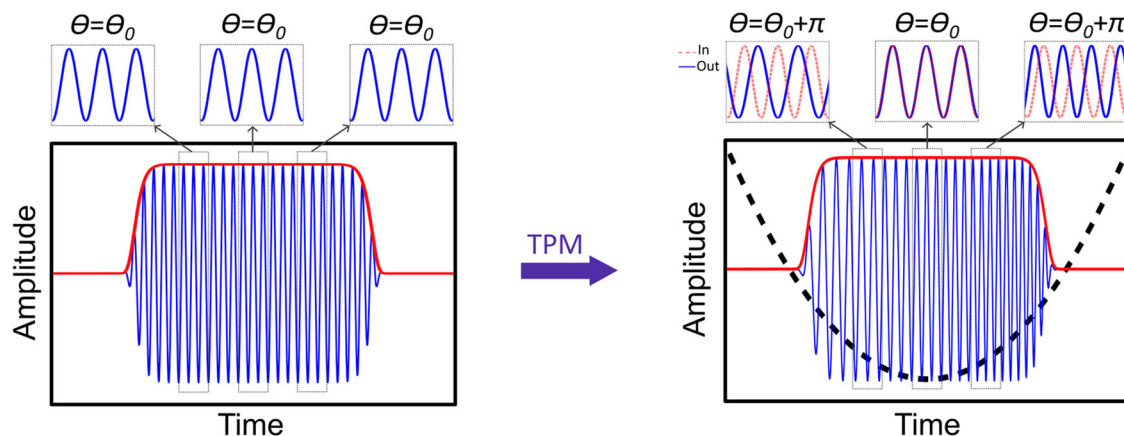


**Fig. 3 | Illustration of Temporal Phase Modulation (TPM) process for the special case of a time lens.** The device implementing a phase transformation changes in optical path length over time from the perspective of the incoming signal. The optical wave profile at three different time locations along the enveloped optical carrier is shown above the input. After implementing the quadratic TPM, shown in black dotted lines, the optical wave will be given a phase depending on the time of arrival.

At the output, the optical wave shown with a blue solid line exhibits a different relative phase in comparison to the input optical wave, overlaid as a red dashed line. The centre of the time lens, experiencing no phase shift, stays coherent relative to the input. The change in periodicity seen in the zoomed sections represent the actual linear instantaneous frequency shift that is being performed, but is greatly exaggerated for clarity.

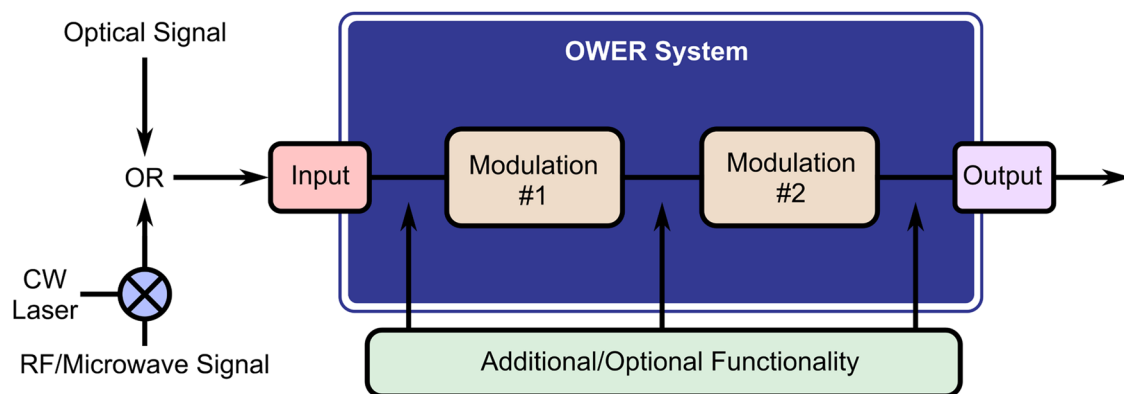


**Fig. 4 | Illustration of the basic structure of an OWER system.** An input signal to be processed may be in the form of an optical, RF, or microwave signal. In the case of an RF or microwave signal, the electronic signal must first be modulated onto an optical carrier from a continuous wave (CW) laser. Once the signal is on an optical carrier, it is ready for the OWER system processing. The most basic implementation may consist of one or two linear optical phase modulations. For the majority of the techniques discussed in this paper, these are TPM and SPF. The order of the

modulations, TPM then SPF or SPF then TPM, is determined by the desired functionality. Additionally, including other transformations such as intensity modulation at any point in the process can provide more functionality and implement a wider variety of techniques such as noise filtering or passive logic. The output of the OWER system can be converted back into the electrical domain, further analysed by optical methods, or even sent to additional OWER systems.

quadratic phase shift depending on time<sup>27,29</sup>. Mathematically, the relative temporal phase shift  $\varphi(t)$  can be written as,

$$H(t) = e^{i\varphi(t)} = e^{\frac{C_L}{2}t'^2}, \quad (2.8)$$

where  $t' = t - t_0$  is the shifted time with respect to the centre of the lens, and  $C_L$  is a parameter defining the curvature or focusing power of the lens. This parameter defines the slope of the instantaneous frequency variation, or chirp, over time that is imparted to the wave due to the phase shift (instantaneous frequency is defined here as the derivative of the temporal phase<sup>30</sup>). The product of the temporal width over which the modulation is applied, or temporal aperture, along with  $C_L$  determine the bandwidth of the time lens, equivalent to the difference between the lowest and highest instantaneous frequency shifts. Figure 3 shows a TPM according to a time lens for a certain input wave consisting of an enveloped optical carrier. The figure is illustrative in nature, and thus exaggerates the instantaneous frequency shift, seen as a change in the period of the optical carrier oscillations at the output over time.

Finally, notice the similarity in form of Eq. (2.8) with Eq. (2.6). It is this similarity that connects TPM and SPF in the theory of temporal imaging<sup>27,29</sup>. Combining SPF and TPM into a single linear system as in Fig. 4 can provide key processing functionalities such as spectrum analysis which will be the subject of Chapter 3.

### Implementations

In practice, a linear SPF system of an optical wave can be implemented using a large variety of physical mechanisms based on free-space optics, fibre-optics, and optical waveguide devices and technologies<sup>23,25,26</sup>. A convenient way of implementing SPF involves the use of a so-called optical pulse shaper<sup>23,31</sup>, where a target spectral phase shift profile can be electronically programmed and imposed on the input light wave. Optical pulse shapers are commercially available that can operate over a very large range of frequencies (operation bandwidth), easily extending over tens of THz and with frequency resolutions down to ~10 GHz<sup>32</sup>, ultimately limiting the amount of GVD that can be emulated to a maximum of 100 ps/nm per 50 GHz channel.



As discussed above, quadratic SPF can be easily implemented using GVD. In the optical domain, this process occurs naturally in the standard single-mode fibres (SMF) that are routinely used for optical telecommunications. GVD is known to represent a key impairment for high-speed communications<sup>26</sup>. Several technologies have been developed to compensate for the dispersion (GVD and higher-order terms) introduced by fiber links. These technologies are designed to provide a spectral phase response (or group delay profile) identical in magnitude but opposite sign to that of the optical fibre to be compensated for. As such, optical GVD compensation in optical fibres in fact represents one of the most fundamental and simple examples of optical processing methods based on the OWR principle. An important consequence of the development of optical GVD compensation is that there is a wide range of available technology alternatives for the implementation of a desired amount of GVD, including dispersion compensating fibres (DCFs)<sup>26</sup>, linearly chirped fibre Bragg gratings (LC-FBGs)<sup>33,34</sup>, integrated optical waveguide devices<sup>25,35–37</sup>, arrayed-waveguide gratings<sup>38</sup>, wavelength-selective switches<sup>38</sup>, and many others. Many of these devices are able to compensate the GVD equivalent of hundreds of km of SMF. LC-FBGs are particularly interesting as these are fibre-optics devices based upon specially designed micro-structured gratings photo-inscribed inside an optical fibre that can be designed to provide a very large GVD coefficient in a very compact format<sup>34,39</sup>. In particular, there are techniques for writing highly compact LC-FBG devices (mm physical lengths) operating over hundreds of nm of bandwidth<sup>40</sup>, but with relatively low overall chirps. On the other hand, there are techniques which have shown that LC-FBGs can be fabricated over a meter long<sup>41</sup>. Commercially available devices such as those from Proximion are able to provide tens of ns/nm chirp rates over 6 nm bandwidth<sup>42</sup>, or less chirp for larger bandwidths up to 40 nm, both compensating for hundreds of km of dispersion in SMF. Customized SPF, including GVD, has been demonstrated using in compact integrated-waveguide implementations, including discrete phase filters, arrayed waveguide gratings, and ring resonators, as detailed further in Chapter 8.

TPM can be efficiently implemented on optical waves using the Pockels effect. Although the Pockels effect is a manifestation of the second order nonlinear susceptibility tensor, it is considered a linear electro-optic phase modulation (EOPM) because the index of refraction of a suitable crystal, lithium niobate (LiNO<sub>3</sub>) for example, placed between metal plates varies linearly with the electric field strength between those plates<sup>15,43</sup>. From the perspective of the optical wave being modulated, as long as the intensity is not sufficiently high as to introduce unwanted higher order nonlinear effects in the crystal, there will be no dependence on the input optical field strength. Note in this situation, aside from the unavoidable coupling loss and loss from material non-idealities, all the optical energy input into the crystal will make it to the output, thus conserving the energy of the signal. Linear EOPMs based on the Pockels effect are commercially available with RF modulation bandwidths from DC to 100 GHz. An arbitrary waveform generator (AWG) can be used to generate any desired driving electrical signal with bandwidths up to 100 GHz, thereby producing any desired phase modulation up to that bandwidth. A common, simple way to produce time lenses according to Eq. (2.8) is to approximate them using the troughs of a sinusoidal modulation, requiring only an RF synthesizer<sup>44</sup>. In this case, the period of the sinusoidal modulation should match the repetition rate of the pulses being analysed. It is also possible to implement TPM using higher order nonlinear optics effects such as four-wave mixing<sup>45–47</sup> and cross modulation<sup>48</sup>, which are capable of significantly faster modulations since they are based on nonlinear interactions with another optical wave, rather than a bandlimited RF wave or microwave. However, nonlinear TPM methods trade speed for energy efficiency, and are notoriously power-hungry<sup>26</sup>. More compact on-chip implementations (discussed in Chapter 8) include plasmonic resonators<sup>49</sup> and thin-film lithium niobate<sup>50</sup>, which have the potential to lower losses, latency, and increase speed.

Finally, it is pertinent to note that there are many more methods still of implementing phase modulation functions by moving into the domain of free-space optics. The analogy between diffraction in space and dispersion in

time for optical light is known as the space-time duality<sup>27</sup>. In particular, the analogue of TPM is spatial phase modulation (SPM), while the analogue of SPF is free space diffraction (FSD). The same principles of energy redistribution apply, and by combining SPM and FSD, a wide variety of image processing functionalities can be implemented<sup>51</sup>. Two examples of this are using a machine-learning algorithm to create a spectral phase mask for the purposes of optimizing a femtosecond laser source<sup>52</sup> as an extension of pulse shaping techniques<sup>31,53</sup>, or creating many consecutive spatial phase masks to mimic the layers of a deep neural network<sup>54</sup>. The interest in using optics for implementing machine learning algorithms and neural networks is similar to the motivations of photonic processing for temporal signals, namely, potential decreased energy requirements, lower latency, and the faster treatment of larger amounts of data. As mentioned, the focus of this review will be on TPM and SPF for one-dimensional, temporal signals. Optical neural networks have also been described in the time domain<sup>55,56</sup>, and are briefly discussed in Chapter 5 on other functionalities. In principle, space-time duality<sup>27</sup> suggests that all temporal signal processing methods and techniques to be discussed have analogues in the spatial domain, and vice versa. This motivates investigation into both domains to find novel and unreported phenomenon that can be transferred between each.

## Real-time Spectral Analysis

Spectral analysis refers to the measurement and detection of a signal's frequency content. It is key for applications including communications, radar, and sensing systems<sup>18,57</sup>. In a controlled environment, spectral measurements can be repeated and there is plenty of time to analyse the results. However, in many real-world applications such as automotive systems<sup>14</sup>, astrophysics<sup>58</sup>, or defence<sup>59</sup>, signals of interest can occur only once, and responsive action must be taken immediately. If this signal cannot be reproduced on demand, then the acquisition must be performed in a single-shot manner, which means that the complete analysis must be done on a single instance of the signal of interest. Real-time spectrum analysis (RT-SA) means that the processing is completed as fast as the signal of interest is arriving, preferably with a latency (input-to-output delay) as low as possible. DSP-based methods, such as fast Fourier transform (FFT)-based algorithms, are commonly used for RT-SA. These DSP techniques offer flexibility and high resolution but can suffer from high computational complexity, leading to increased latency in large-scale implementations and applications involving large instantaneous bandwidths<sup>60</sup>. In contrast, this chapter will focus on the description of two state-of-the-art, single-shot, photonic RT-SA techniques known as the time lens spectrogram (TLS) and the Talbot array illuminator spectrogram (TAIS). These techniques only require the SPF and TPM transformations discussed in the previous chapter, and are therefore completed entirely in the analogue optical domain, bringing all the advantages of low latency and energy efficiency. First however, the simplest implementation of RT-SA will be introduced, involving a single SPF on a time-limited waveform.

## Dispersive Fourier Transform

A main strategy for spectral analysis relies on mapping the spectral intensity distribution of an optical wave along the time domain, known as a time-mapped Fourier transform (TM-FT)<sup>29,61–67</sup>. A dispersive Fourier transform (DFT) is the technique involving just a single SPF step, specifically, a GVD of exactly the type discussed in Chapter 2. Recall for GVD, the group delay varies linearly with frequency. Therefore, when a temporally short waveform is transmitted through a dispersive medium having a sufficiently large amount of GVD ( $\phi$ ), the different frequency components of the propagating signal are effectively separated along the time domain. It is then the frequency spectrum of the signal that is directly mapped along the time-domain (i.e. Fourier transform by frequency-to-time mapping). The DFT is based on the analogy between the paraxial diffraction of free space optical beams in the far-field (Fraunhofer) regime and the dispersive propagation of temporal waveforms<sup>29,65</sup>. Therefore, the dispersion amount should satisfy the so-called temporal Fraunhofer condition<sup>29,65–67</sup>,  $|\phi| \gg t_w^2/(2\pi)$ , where  $t_w$  is the temporal duration of the signal of interest. The frequency axis is then

mapped along the temporal axis of the output waveform following the scaling law

$$\omega_t = \frac{t}{\phi}, \quad (3.1)$$

where  $\omega_t$  is the input frequency variable relative to the signal's central carrier frequency and  $t$  is the output time variable relative to the centre of the output waveform. The time-mapped spectrum can then be directly recovered with a photodetector and analysed in a real-time, single shot fashion. The DFT approach allows for capturing spectral information over large instantaneous bandwidths ( $> \text{THz}$ ) through time-domain instrumentation with measurement update rates well in the MHz or even GHz regimes, but the frequency resolution is typically sacrificed for high refresh rates. Although this approach is simple and promising for spectral analysis over large bandwidths, it is constrained to time-limited short pulses ( $\sim \text{ps}$  or  $\sim \text{fs}$  durations) since more GVD is needed to separate the bandwidth and provide an adequate sampling of the spectrum at the output. Additionally, the output temporal waveform (time-mapped spectrum) is necessarily much longer than the input one. Thus, the time-limited waveforms, or pulses, to be analysed must be spaced apart by a long temporal period.

To overcome the limitations of pulse width and pulse period, a set of techniques based on temporal imaging, called time lens Fourier transforms, have been developed<sup>29,68–70</sup>. These techniques combine the SPF with TPM to increase user control. The use of a single time-lens for waveform analysis has been demonstrated for time-to-frequency mapping<sup>71</sup>, enabling the measurement of a high-speed waveform through a frequency-domain measurement. However, in the context of RT-SA, temporal imaging approaches most typically involve the use of dispersive lines in addition to the time-lens manipulation. For instance, a time-lens Fourier transformer can be designed using the temporal analogue of the two-focal-length ( $2f$ ) spatial lens system (i.e., two dispersive elements separated by a time lens), or the one-focal-length ( $1f$ ) spatial lens system (i.e., a time-lens followed by a single dispersive line). These methods differ in their achievable analysis bandwidth, compactness, and experimental simplicity, and for a comprehensive review, the reader is referred to Salem et al.<sup>29</sup>. Generally, these methods have the advantage that the spectral phase profile is also mapped to the time domain<sup>68</sup>, in contrast to DFT, where the phase profile is severely distorted. Furthermore, time-lens FT methods allow for the measurement of significantly longer signals ( $\sim \text{ns}$ )<sup>72</sup>, limited by the duration of the time lens, which is in turn typically constrained by the achievable phase excursion of the phase modulation process<sup>29</sup>. Furthermore, the spectral analysis of signals of longer durations necessitates sharper frequency resolution. Time-lens FT methods also lead to an output frequency-to-time mapped spectrum that is significantly shorter than those obtained by DFT, which is particularly useful for the analysis of high repetition rate pulsed waveforms<sup>70</sup>. The development of alternative methods to increase both the frequency resolution and the maximum duration of the signal under test (SUT) while maintaining a broad analysis bandwidth remains an active field of research. This includes for instance the use of loop structures allowing for kHz frequency resolutions<sup>63</sup>, using chirped broadband waveforms for the needed quadratic temporal phase variation instead of an electro-optic (EO) time lens<sup>73</sup>, and sampling on a train of pulses<sup>64</sup>.

Even though the time-lens Fourier transformer allows the processing of a more general class of signals than the DFT, both methods are inherently restricted to treating time-limited waveforms, such as short pulses. However, many important applications demand the real-time, single shot spectral analysis of continuous waveforms, such as in the fields of sensing and ranging<sup>74</sup>, spectroscopy<sup>75</sup>, and telecommunications<sup>76</sup>. It is possible to chop a continuous signal into many time-limited segments, and then perform either time-lens FT or DFT on each segment. This allows one to obtain information on the signal's spectrum as it evolves over time, as long as the segments are sufficiently divided and separated from one another<sup>77</sup>. Rather than multiply the number of analysis systems to match the division of segments, there are techniques which discard most of the segments and simply assume the spectrum is evolving slow enough such that analysing

only periodic sections is justified<sup>66</sup>. However, these methods necessarily suffer from large gaps in the analysis which is often unacceptable if short transient events are involved<sup>78</sup>.

### Time Lens Spectrogram

To address the applications requiring real-time, single shot spectral analysis of continuous varying signals extending over arbitrarily long time durations, alternative schemes have been proposed, in which the analysis is performed in an entirely dynamic and gap-free manner<sup>61,79–81</sup>. However, it has been challenging to extend the operation bandwidth of these methods over a few GHz. Here we review two photonic-based analogue processing approaches based on the OWER principle that have allowed for the analysis of broadband and time-continuous signals ( $> 10 \text{ GHz}$ ) through time-mapped spectrogram techniques. A spectrogram provides a joint time-frequency (TF) distribution of a SUT, representing the variation of the signal energy as a function of the two variables, time and frequency simultaneously<sup>30,82</sup>. This is calculated as the squared magnitude of a short-time Fourier transform (STFT), in which adjacent or overlapping temporal sections of the SUT are consecutively Fourier transformed.

We first discuss the time lens spectrogram (TLS)<sup>82</sup>, which can provide very large operation bandwidths (sub-THz) and high temporal resolutions (tens of ps), although with a relatively limited number of analysis points per spectrum ( $\sim 10\text{--}30$ )<sup>30,72</sup>. In contrast to the array of time lenses generated using a sinusoid from an RF synthesizer, the TLS is based on the implementation of consecutive quadratic time-lenses generated by an AWG. As a result, the TLS consists of lenses placed edge-to-edge, with no gaps. After the lenses, the dispersion is chosen to match the spectral phase induced by each individual time lens, similarly to the time-lens FT mentioned above. The maximum signal bandwidth is then set equal to the time-lens bandwidth, such that the output spectra are mapped within the temporal width of the time lenses, and therefore do not overlap with neighbouring spectra. This method mathematically corresponds to an STFT, with adjacent, non-overlapping temporal analysis windows<sup>82</sup>.

The fundamental principle behind the TLS is shown in Fig. 5a. A linearly chirped signal, here taken as an example input signal to be analysed, is first sent to a set of consecutive quadratic time-lenses. This is then followed by a second-order dispersive propagation. Following the TPM and the SPF, the consecutive spectra of the SUT are effectively mapped along the time domain. The required condition relating the two transformations for a proper Fourier transform is  $C_L \ddot{\phi} = 1$ , meaning the dispersion is inversely proportional to the time lens strength<sup>82</sup>. Finally, assuming the bandwidth of the SUT is less than or equal to the bandwidth of the time lens implemented,  $B_w \leq C_L T_L / 2\pi$ , enables the full spectrum to be mapped within the temporal size of a single lens,  $T_L$ , and mapped linearly over this duration following the same frequency-to-time scaling law as in Eq. 3.1.

Since EO time lenses can be implemented with bandwidths exceeding hundreds of GHz, the TLS allows for the analysis of much broader waveforms compared to other real-time dynamic spectrum analysis methods. As shown in Fig. 6a, EO TLS systems have been demonstrated that can provide over 400 GHz of instantaneous bandwidth<sup>82</sup>, while maintaining a real-time and gapless analysis for continuous signals. The TLS also excels at providing very short time resolutions, demonstrated to below 70 picoseconds<sup>82</sup>. Since the analysis windows are concatenated edge-to-edge, this implies that the time resolution of the obtained spectrogram analysis is determined by the width of the temporal analysis window, namely, the time lens aperture size  $T_L$ . The frequency resolution is inversely related to the time resolution  $\delta f \propto 1/T_L$ <sup>82</sup>. The analysis bandwidth and frequency resolution also determine the number of points for the representation of each of the calculated signal spectra along the analysis window. The TLS is quite flexible in its design parameters, having been demonstrated to produce full instantaneous bandwidths as low as 11.2 GHz with sub-GHz frequency resolution and about a nanosecond of time resolution<sup>83</sup>.

However, the TLS method that can capture the dynamic spectra of signals is limited to around 30 analysis points per measured spectrum<sup>82</sup>. The limitation is mainly caused by the maximum possible phase excursion  $\phi_{\max}$

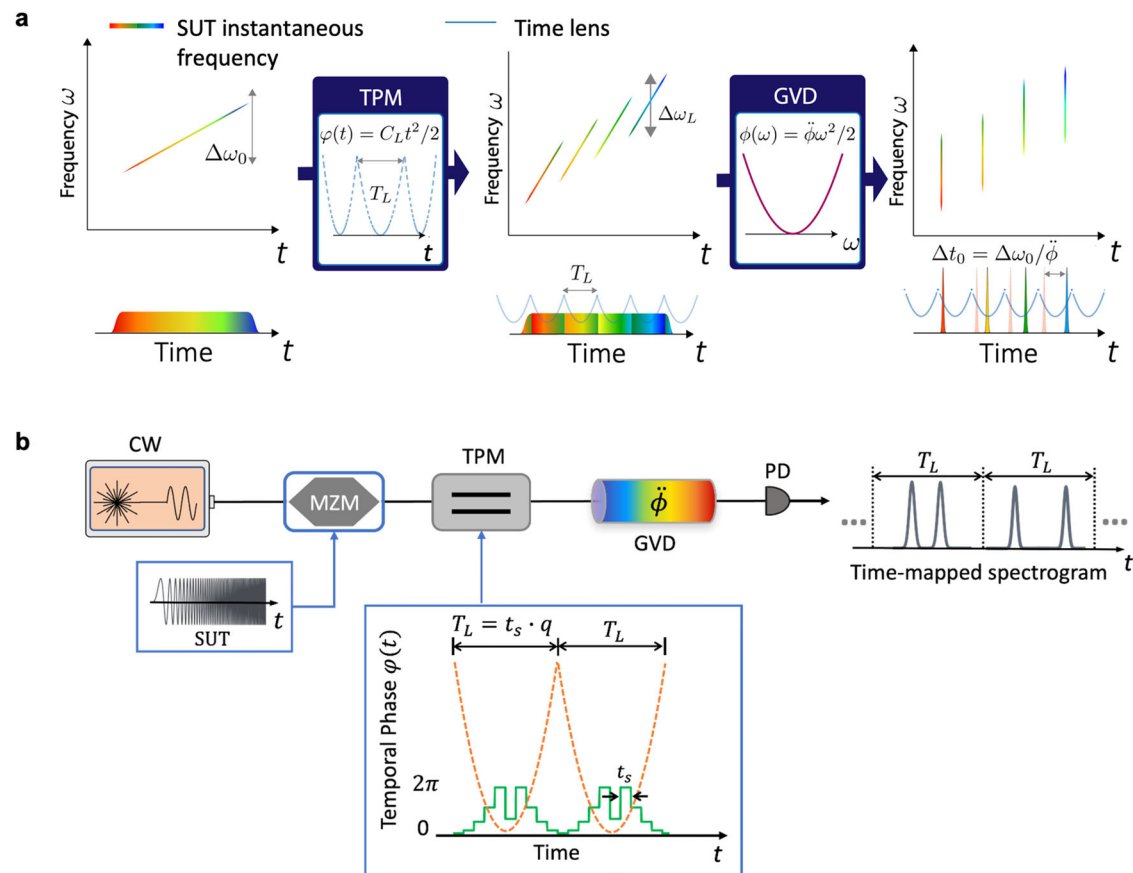


**Fig. 5 | Principle and experimental diagram of the time lens spectrogram (TLS) and Talbot array illuminator spectrogram (TAIS) scheme.** **a** The TLS involves an array of adjacent time lenses followed by GVD to time map the frequency spectrum of each of the temporal sections of the signal under test (SUT) under each time lens aperture along the corresponding temporal slot, ensuring real-time spectral analysis of

consecutive time sections of the SUT in a gapless and continuous manner. **b** The scheme of a real-time spectrogram analysis based on similar principles but using Talbot phase modulation, implementing a TAIS. In the shown example, the scheme is utilized for the analysis of microwave signals (SUT), e.g., as captured by a suitable antenna, by simply modulating this SUT on a continuous-wave (CW) light beam (optical carrier).

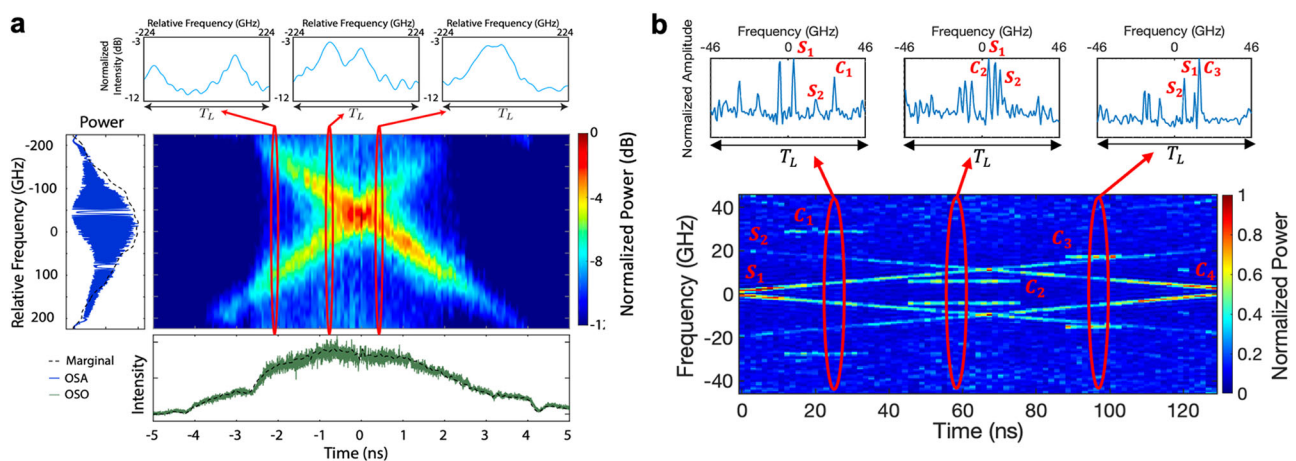


**Fig. 6 | Experimental results for a time lens spectrogram (TLS) and a Talbot array illuminator spectrogram (TAIS).** **a** TLS results for time-frequency analysis of a complex double-chirped optical waveform with bandwidth of 411 GHz<sup>42</sup>. **b** Results corresponding to a TAIS used for the analysis of 40-GHz microwave signal

consisting of a double-chirped signal with single-frequency interferences occurring at different time-frequency locations, illustrating the sharp (sub-GHz) frequency resolution that is offered by this method while enabling to capture nanosecond events.

of the temporal phase modulation. Specifically, the number of analysis points per output spectrum can be estimated as  $N \approx 4\phi_{\max}/\pi$ . For EOPMs, the maximum total phase excursion is typically around  $7\pi$ . This can be a significant issue for recovering highly complex spectra, as the frequency resolution may not be sufficient to discern closely spaced frequency features.

### Talbot Array Illuminator

The second method combining TPM and SPF, aimed at addressing the limitation of analysis points, is the Talbot array illuminator spectrogram (TAIS). As depicted in Fig. 5b, the TAIS is based on a discrete and wrapped phase that is determined by the framework of the temporal Talbot array



illuminator<sup>84–87</sup>. Recent work has also shown that within certain conditions, the TAI phase modulation can be also interpreted as a discretized and bounded version of an array of time lenses<sup>88,89</sup>. Each temporal phase modulation profile consists of a discrete pattern composed of  $q$  levels (green, solid curve), each over a duration of  $t_s$ , where the  $n^{\text{th}}$  phase step satisfies:

$$\varphi_n = -\frac{\pi n^2(q-1)}{q}, \quad (3.2)$$

where  $n = 1, \dots, q$ . The phase shifts in Eq. (3.2) can be practically implemented using the equivalent modulus  $2\pi$  phase, which limits the maximum phase excursion to  $2\pi$  while implementing a manipulation equivalent to that of a conventional time-lens with a large phase excursion (orange dashed line). The phase modulated signal then propagates through a dispersive medium providing a GVD  $\phi$  satisfying,

$$2\pi|\ddot{\phi}| = qt_s^2. \quad (3.3)$$

Consequently, the frequency content of the SUT is analysed over successive temporal sections, each with a duration of  $T_L = qt_s$ , and is consecutively mapped along the time domain following Eq. (3.1). The resulting full analysis bandwidth is given by the inverse of the duration of a single phase step, i.e.  $1/t_s$ , while the temporal resolution is approximately given by the period of the phase pattern  $T_L$ , which is again inversely related to the frequency resolution<sup>85,86</sup>. The total number of analysis points per mapped spectrum corresponds to the number of the modulation phase levels  $q$ . As such, this design enables the realization of hundreds of analysis points, well beyond the capabilities of the TLS method.

Figure 5b illustrates an experimental demonstration of the TAIS<sup>86</sup>. The input optical SUT is first modulated by the TAI phase, which can be implemented with an EOPM device. Subsequently, the phase-modulated SUT propagates through a linear dispersive line providing the required GVD. The resulting temporal signal corresponds to consecutive time-mapped spectra within each period  $T_L$  after the photo-detection. This system enables the analysis of high-speed microwave signals by simply modulating the SUT on a continuous wave (CW) light beam. This scheme has been successfully demonstrated for real-time spectrogram analysis of arbitrary signals with full bandwidth up to 92 GHz<sup>84</sup>. Figure 6b shows the 2D representation of the resulting time-mapped spectrogram of a SUT composed of a two-chirped signal and isolated interferences with varying frequency content and temporal durations<sup>90</sup>. The figure includes three different zoomed-in regions showing the time-mapped spectra of different analysis periods, corresponding to some of the interference locations. The main limitation of the TAIS for improving frequency resolution even further is the large amount of GVD required. Hundreds of analysis points can be achieved, but this requires hundreds of kilometres of SMF-equivalent GVD<sup>84</sup>.

## Discussion

For both the TLS and the TAIS, the signal of interest may be an optical wave, or an electrical (microwave to mm-wave) signal upconverted onto an optical carrier. These methods are real-time, single shot, and gapless spectral analysis techniques with unprecedented speed and bandwidth, as required for applications such as for software-defined radar, cognitive high-speed communications, and the recovery of complex modulation telecommunication signals<sup>18,76,82,91</sup>. Finally, it is worth emphasizing that the spectrum of the input SUT is directly mapped along the time axis in the original physical wave domain, enabling direct access to the time-frequency distribution of the signal in a real-time manner. This allows for the use of well-established time-domain waveform modulation and manipulation methods to implement a user-defined time-frequency filtering operation, such as a target ultrafast reconfigurable filter<sup>90</sup>. A key consideration for this application is that the frequency-to-time mapping process is implemented using linear phase-only transformations. As such, the filtered signal can be recovered through the inverse transformations (i.e. the same OWER system

backwards and with opposite sign). This provides a possibility to manipulate the signal dynamically and can offer unprecedented capabilities across a wide range of applications.

## Denosing and Passive Amplification Methods

The problem of noise is significant in almost all scientific fields and real-world applications. Specifically in optical systems, amplified spontaneous emission (ASE) noise can corrupt the accurate retrieval of information in applications such as microwave photonic links<sup>92</sup>, LiDAR<sup>93</sup>, communication systems<sup>94</sup>, and spectroscopy<sup>95</sup>. Noise (random disturbances affecting amplitude and/or phase) can originate from various sources, including from thermal effects, ASE, or background ambient light<sup>15,96</sup>. Whereas optical amplifiers like erbium-doped fibre amplifiers (EDFAs)<sup>97</sup> and fibre-optic parametric amplifiers (FOPAs)<sup>98</sup> are typically employed to boost the signal's intensity, they also indiscriminately amplify pre-existing noise and introduce additional noise (e.g., ASE), thereby degrading the signal-to-noise ratio (SNR). For this reason, amplification and noise mitigation are two closely related operations. While the use of amplifiers is ubiquitous, noise mitigation strategies strongly vary depending on the signal's characteristics. As a precursor to denoising and passive amplification, we review past developments in controlling optical pulse rates, or the frequency spacing of the related optical frequency combs, with TPM and SPF.

### Lossless Pulse Rate and Frequency Comb Spacing Control

Controlling the repetition rate of periodic optical waveforms or the frequency spacing of their spectral representation (typically referred to as optical frequency combs)<sup>99</sup>, is an indispensable functionality for a large number of applications, including ultrafast optical and microwave signal generation and processing<sup>16,17,100,101</sup>, high-resolution spectroscopy<sup>102–104</sup> and frequency metrology<sup>105–107</sup>, high-capacity telecommunication systems<sup>108,109</sup>, as well as for quantum information processing and computing<sup>110</sup>.

Lossless pulse rate control methods are most typically based on the temporal Talbot effect<sup>111–117</sup>, a set of self-imaging phenomena that also form the basis of the TAIS discussed in Chapter 3. The Talbot effect is observed when a periodic temporal waveform undergoes second-order GVD, such as in the case of a periodic optical pulse train propagating through a dispersive fibre, and for specific well-defined amounts of dispersion relative to the waveform repetition period, the original pulse train is replicated with the exact same repetition rate (integer Talbot phenomena). The amount of dispersion can also be a fraction of the integer amount, in which case the original pulse train is replicated with a repetition rate that is an exact integer multiple of the input one (fractional Talbot phenomena). In this latest case, the rate-multiplied pulses exhibit pulse-to-pulse phase shifts that follow a precise well-defined profile, what is usually referred to as a Talbot phase profile<sup>118</sup>. Using these fundamental principles, it has been shown that the repetition rate of a given periodic waveform can be modified at will through a suitable combination of Talbot phase modulation and GVD applied on the input pulse train<sup>119,120</sup>. As this method is based on TPM and SPF, the overall energy of the input pulse train is maintained throughout the OWER process. Therefore, in the case of repetition rate division, the overall energy of the pulse train is split among a smaller number of pulses leading to an effective energy increase, i.e., passive amplification, of each of the individual waveforms in the output train<sup>119</sup>. It was also observed that this passive amplification effect was applied only to the periodically repeating components of the signal, ignoring any other non-repeating components such as incoherent optical noise<sup>119</sup>. The effect of passive amplification was first proposed and experimentally demonstrated in this context and later extended to the case of arbitrary, generally non-periodic, waveforms, as described in the following section.

Note that the spectral representation of a periodic temporal waveform is also a periodic function of frequency, namely, an optical frequency comb<sup>100</sup>. As such, arbitrary control of the frequency spacing of the comb can be also achieved using the equivalent SPF and TPM transformations on the original pulse train<sup>99,121–124</sup>. Similarly, increasing the comb frequency spacing enables passive amplification of the frequency comb lines over any non-



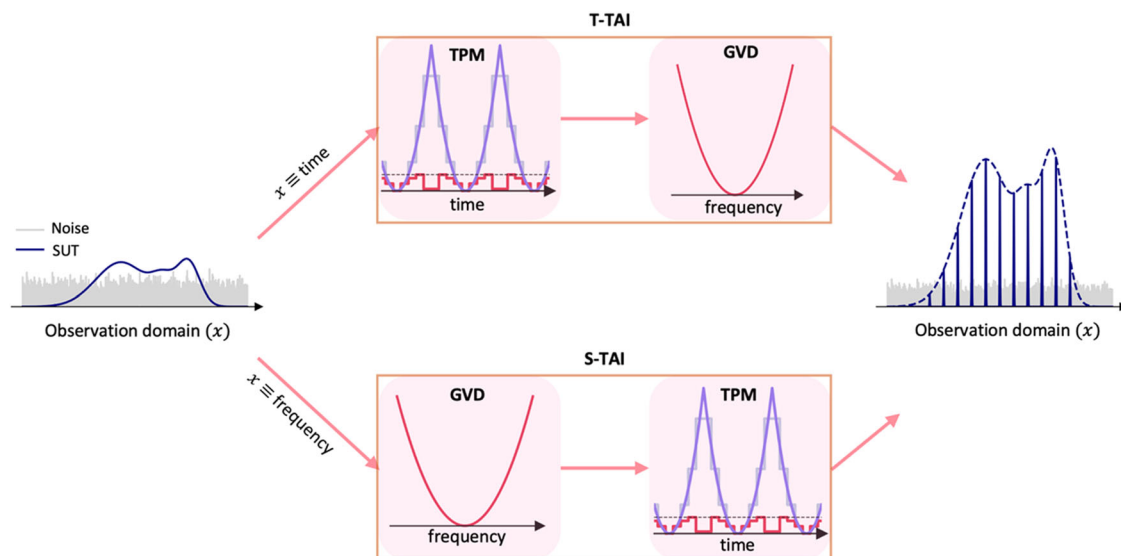


**Fig. 7 | Schematic of noise mitigation systems using a T-TAI and an S-TAI.** The top row illustrates the T-TAI, which involves TPM of the signal under test (SUT) with a quadratic periodic phase pattern derived from the Talbot effect, followed by quadratic spectral phase filtering via GVD. This process focuses the waveform energy into short temporal pulses, resulting in an effective local amplification by a

magnification factor of  $q$ . The bottom row shows the S-TAI, which starts with GVD and is followed by TPM, achieving similar amplification effects along the spectral domain. In both methods, the phase-coherent target signal is locally amplified, while noise remains nearly unaltered.

repeating components, such as background noise<sup>99,125</sup>. Examples of denoising passive amplification of periodic pulses and optical frequency combs using these methods are shown in Fig. 8 and described in the following section.

Talbot-based processing of optical pulses and frequency combs have been extensively demonstrated and applied. The reader is addressed to Cortéz et al.<sup>99</sup>, which provides a comprehensive review of this field. In practice, the minimum rate or frequency spacing that can be manipulated using these methods is limited by the fact that the needed amount of GVD scales up with the square of the input or output temporal pulse period. Therefore, these solutions are mainly suited for processing optical pulses and frequency combs with frequency spacings of a few GHz at least. Talbot processing has enabled the generation of THz rate optical pulse trains from GHz and even sub-GHz rate pulse trains<sup>117</sup>. On the other hand, rate division processes are limited by the need of temporal phase modulations as fast as the input pulse rate, namely, to a few tens of GHz using EOPM mechanisms.

### Temporal and Spectral Talbot Array Illuminators

For the purposes of treating noise, we categorize optical signals into two overarching groups: narrowband signals<sup>9</sup>, with slow temporal variations and bandwidths below the GHz range (e.g., vibration monitoring, bio-sensors, LiDAR, microwave photonics, telecommunications), and broadband signals<sup>79</sup>, with frequency ranges over tens of GHz, typically associated with short pulses (e.g., ultrafast processes, spectroscopy, radio astronomy, bioimaging).

Narrowband signals lend themselves to conventional filtering techniques using optical band-pass filters (BPFs) based on Fabry-Perot cavities, Fibre Bragg Gratings (FBGs), or microring resonators, among others, since in this case, most of the noise is outside the signal's frequency band<sup>126</sup>. Unfortunately, building BPFs with sub-GHz passbands poses significant challenges, including the necessity to precisely align the BPF passband with the frequency of the signal of interest, which may be unknown or dynamically fluctuate. Alternatives based on the stimulated Brillouin scattering (SBS) effect have been exploited to create narrowband optical filters, but these approaches are mostly suitable for microwave photonics applications where the laser source is controlled by the user<sup>127–129</sup>. On the other hand, noise mitigation in broadband signals is challenging due to most of the noise being within the signal's bandwidth. Some advances in the mitigation of in-

band noise include the use of matched filters<sup>130</sup> and spatio-spectral filtering<sup>131</sup>, both of which rely on having prior knowledge of some of the signal's parameters. Solutions for mitigating in-band noise through digital signal processing (DSP) have been proposed in the realms of acoustic and radio-frequency signals<sup>132–134</sup>, but they are not suitable for aperiodic ultrafast optical signals due to the significant challenge posed by the digitization of broadband complex optical fields.

Noise mitigation based on passive amplification was initially demonstrated for periodic pulse trains as described in the previous section<sup>135</sup>. Subsequently, the dual effect was observed in the frequency domain for frequency combs<sup>136</sup>. A simultaneous spatial and temporal focusing has also been demonstrated for femtosecond pulses to improve the performance of multiphoton microscopy and medical imaging<sup>137</sup>. More recently, the concept has been generalized for arbitrary continuous input signals, as detailed in what follows.

Figure 7 presents the schematic of a system used for noise mitigation in arbitrary narrowband optical signals, known as the Temporal Talbot Array Illuminator (T-TAI)<sup>19,87</sup>. Similar to the TAIS, the T-TAI begins with a TPM according to the TAI pattern of Eq. (3.2), bounded once again to  $2\pi$ . After TPM, a quadratic SPF is applied according to Eq. (3.3). The link to the optical pulse control from the previous section is that an arbitrary signal can be thought of as a limiting case when the pulse width equals the pulse period<sup>138</sup>, which is much shorter than the arbitrary waveform's duration, corresponding to the envelope of these virtual pulses. Each "optical pulse" is then given a different phase according to the TAI pattern, and the repetition rate can be divided by  $q = T_L/t_s$  as in Fig. 7. The same energy conservation applies, and the output peaks outline a copy of the input signal amplified by the factor  $q$ . This is very similar to the interpretation of the T-TAI as a temporal counterpart to a periodic optical lens system, which focuses the energy of the illuminating light into equally spaced spots on the focal plane. At these spots, the peak power of the output is linearly proportional to the input waveform, by an amplification factor  $q$ , passively increasing the signal locally within the extent of the spot. Indeed, this coherent sampling operation was first demonstrated using an RF tone to drive the TPM, implementing an array of time lenses, but this approach results in a relatively modest amplification factor of 3.6<sup>139</sup>. Connecting with the TAIS of Chapter 3, if the signal envelope is slowly varying in comparison to the TAI repetition period  $T_L$ , then the TAIS process results in single pulses for each

pattern representing a DC frequency component with no other spectral features, whose amplitude depends on the amplitude of the signal within the pattern period<sup>82</sup>. If the noise is broadband, then using the TAI framework it is easy to see why the phase-coherent signal of interest focuses to a single peak while the broadband noise is mapped along a much longer time duration. The T-TAI has been demonstrated experimentally for passive amplification and noise mitigation of both periodic optical pulse trains and continuous arbitrary temporal waveforms, such as microwave photonic signals (e.g., sinusoids modulated on optical carriers) and optical telecommunication data streams. The T-TAI method achieved amplification factors greater than 100, which enabled the recovery of ultra-weak optical signals with power levels below the detector threshold, buried under a much stronger noise background<sup>19</sup> (noise power more than 30 times higher than the signal). Examples of denoising passive amplification of an optical pulse train and a narrowband square-like temporal pulse are shown in Fig. 8a, b, respectively. By using high amplification factor  $q = 120$ , effective filtering passbands of about 320 MHz has been achieved with the T-TAI system.

Interestingly, similar phenomena can be achieved along the frequency domain representation of the SUT using a system known as the Spectral Talbot Array Illuminator (S-TAI)<sup>19</sup>. The S-TAI achieves passive amplification along the frequency domain by redistributing the energy into spectral peaks, rather than along the time domain, and can be immediately generalized to arbitrary waveforms similar to the T-TAI. The way to realize the S-TAI is simply to reverse the TPM and SPF. This system is particularly effective for noise mitigation in broadband signals affected by in-band noise. S-TAIs have been demonstrated experimentally for the passive amplification and noise mitigation of both periodic optical frequency combs (Fig. 8c) and ultrabroadband arbitrary optical waveforms<sup>99</sup> (Fig. 8d). The S-TAI enabled the real-time and single-shot recovery of broadband optical waveforms with picosecond resolution, even when the signals were buried under in-band noise. This was demonstrated with waveforms extending over a full-width frequency bandwidth up to  $\sim 400$  GHz, corresponding to temporal variations as fast as  $\sim 2$  ps. The system demonstrated significant noise mitigation capabilities, increasing the visibility (a measure of signal detectability) by 18 dB, almost two orders of magnitude (see Fig. 8d).

### Hardware Challenges

Specific to the T-TAI and S-TAI, there are practical implementation challenges to overcome. For the SPF stage, third-order dispersion effects can become non-negligible for broadband signals<sup>140</sup>, as fabricating devices such as LC-FBGs with constant GVD over THz bandwidths is challenging<sup>141</sup>. For the TPM, applying such a sophisticated phase pattern as the TAI may

demand bandwidths that are currently unachievable for state-of-the-art digital-to-analogue converters. For example, to use the T-TAI for the passive amplification of high-speed telecommunication waveforms of tens or hundreds of Gbaud/s, the TAI pattern would need to be much faster than the telecom symbol rate. A significant trade-off exists between the achievable amplification  $q$ , and the phase modulation period  $T_L$ . To overcome this, it becomes necessary to leverage the nonlinear optical processes mentioned in Chapter 2. For instance, ultrafast TLs have been implemented by exploiting cross-phase modulation (XPM) and four-wave mixing (FWM)<sup>29</sup>.

Recently, innovative methodologies have been developed leveraging nonlinear XPM and FWM in optical fibres to achieve an ultrafast implementation of the required TPM, surpassing the speeds achievable through EO approaches by orders of magnitude. An XPM-based discrete-multilevel TPM was first demonstrated through a tailored pulse-shaping process, wherein a pump with an intensity profile proportional to the required TPM is engineered<sup>88</sup>. This approach has been demonstrated in the context of a T-TAI<sup>142</sup> and S-TAI<sup>143</sup>, and a Talbot amplifier for periodic pulses<sup>144</sup>. Due to its phase restriction of  $2\pi$ , this design requires much less power than a conventional XPM-based parabolic TL<sup>88</sup>. Alternatively, an ultrafast TPM can be achieved using FWM<sup>145</sup>, where in this case the pump is obtained by multiplying the repetition rate of a short-pulse train by an integer factor  $q$  through its propagation in a GVD medium satisfying a fractional self-imaging condition. This process results in a pump with a discrete multilevel phase profile directly proportional to the desired TPM, which is then transferred to the idler through the FWM process. This approach has been applied in the context of a T-TAI<sup>145,146</sup> and in a spectral Talbot amplifier to mitigate noise in optical frequency combs<sup>125</sup>.

### Other Functionalities

The techniques of OWER discussed above, namely RT-SA, optical pulse control, denoising, and passive amplification, are just a small sample of the many functionalities enabled by SPF and TPM. In this chapter, a number of noteworthy examples of OWER implementations are introduced to give more perspective on the potential applications.

TPM and SPF transformations have been designed for the realization of many important operations on data sequences such as those used for communication purposes. For example, dispersion-induced Talbot self-imaging effects have been exploited for accurate recovery of the underlying periodic clock reference from intensity modulated optical pulse sequences (on-off keying data, OOK) at the exact same bit rate of the original data<sup>147</sup> or at a fraction of this rate<sup>148</sup>. Additionally, linear SPF has been used for highly

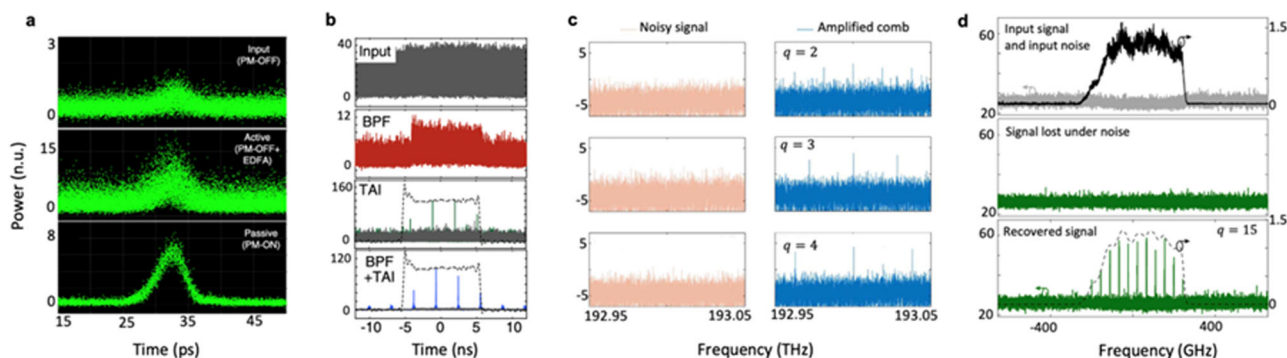


**Fig. 8 | Various realizations of passive amplification using the Talbot effect.**

**a** Noise mitigation of a periodic optical pulse train with amplification factor of 5. Passive amplification is compared with active amplification, with the latter method significantly degrading the signal quality<sup>135</sup>. To evaluate the passive amplification effect beyond the processing system losses, the pulses are measured at the output of the Talbot amplifier when the TPM stage is off (PM-OFF), in which case the output waveform is just an exact copy of the input waveform, and when the TPM stage is on (PM-ON), leading to the anticipated rate division of the input pulse train and the

associated passive amplification effect. **b** Noise mitigation of a narrowband square-like optical pulse using a T-TAI system with  $q = 37$ <sup>14</sup>. The T-TAI method significantly outperforms optical bandpass filtering (BPF). **c** Noiseless spectral amplification of a frequency comb with zero visibility, i.e., when the comb is entirely buried under incoherent noise, for several passive amplification factors<sup>136</sup>. **d** In-band noise mitigation and recovery of a broadband isolated pulsed waveform, which is entirely buried under a significant amount of noise<sup>19</sup>. Figures adapted from<sup>19,44,135,136</sup>.

energy-efficient modulation format conversions of ultrafast optical telecommunication data sequences, such as for conversion of ultrahigh-speed return-to-zero OOK data (in which the data are codified on pulses much shorter than the bit period) and more bandwidth efficient non-return-to-zero OOK data (in which each bit pulse occupies the entire bit period)<sup>149</sup>. OOK data sequences correspond to binary data sequences such as those routinely used for encoding information in DSP engines. Based on this principle, logic functions have been implemented on the binary data encoded on OOK sequences using a well-chosen linear SPF<sup>119,150</sup>. This approach has been referred to as passive logic processing, and it has been successfully used for the implementation of NOT and XNOR logic functions as well as for pattern matching operations<sup>119</sup>. Specifically, a NOT logic operation can be achieved by simply inverting the phase of (or  $\pi$  phase shifting) the central carrier frequency component of the input optical data sequence with respect to the rest of the sequence's spectral content<sup>150</sup>. Passive logic processing has been demonstrated to enable ultrafast processing speeds or binary rates, up to 640 Gbps, well beyond the capabilities of conventional electronic DSP, while avoiding the unpractical power consumption levels of alternative photonic solutions<sup>151</sup>. This functionality offers optimal energy efficiency, particularly when the information is already on an optical carrier, only limited by the practical insertion loss of the phase filter technology, with demonstrated energy dissipations down to a few fJ/bit. Demonstrations have been reported using optical pulse shapers<sup>119</sup> and far more compact FBGs<sup>150</sup> for implementation of the SPF operations.

As mentioned in Chapter 2, optical neural networks have been realized in fiber optics, the backbone of such implementations being OWER methods of TPM and SPF. For example, an iterative process of TMP and SPF create connecting layers of a neural network entirely in the optical domain<sup>55</sup>. The temporal data processing was done in a completely real-time manner with a data rate of 12 Gbps. Contrary to some free space optical neural networks, this fiber-based system is fully reconfigurable. Another example is a convolutional neural network formed by combining SPF with non-energy preserving operations in fiber optics which has been demonstrated for the classification of originally 2D images<sup>56</sup>.

An important aspect of OWER methods emphasized again is that the original input signal energy and information are preserved, allowing for easy recovery of this input signal without any significant loss by simply reversing the implemented SPF and TPM operations. This is the very principle behind optical dispersion compensation in fibre-optic telecommunication systems<sup>33</sup>. Furthermore, this approach enables additional manipulation and processing of the information of interest in the transformed domain before reversal. This principle has been successfully utilized to manipulate at will the time-frequency distribution, or spectrogram, of high-speed signals as described in Chapter 3, as well as to mitigate narrowband noise in microwave signals<sup>152</sup> following the approach described in Chapter 4.

## Quantum-level Implementations

The connection between entangled biphotons and classical pulse shaping was first articulated by Pe'er et al., who showed that the two-photon wavefunction of time-energy entangled photon pairs could be manipulated like a coherent, classical ultrafast pulse<sup>153</sup>. The large impact of this work is evidenced by the number of publications soon after, continuing up through today, that have applied classical signal processing methods using standard telecom equipment on entangled photon pairs. Of the many techniques that have been borrowed from the classical signal processing toolbox, TPM and SPF hold particular importance for quantum processing because they provide a versatile framework that is inherently low loss, a critical requirement for quantum information where signals cannot be amplified<sup>154</sup>. TPM and SPF can be interpreted as unitary transformations on a quantum state (up to the insertion losses of the devices themselves)<sup>155,156</sup>, allowing for important manipulations such as wavefunction shaping<sup>157–161</sup>, quantum state generation and processing<sup>110,162</sup>, and quantum state characterization and detection<sup>21,163–168</sup>.

In this chapter, we will first provide a brief overview on time-energy entangled biphoton wavefunctions in the context of Fourier processing and

then review recent progress pertaining to the application of TPM- and SPF-based OWER manipulations for three key areas: 1) efficient detection of the spectral content of quantum states, 2) improved temporal detection resolution, and 3) noise mitigation.

## Biphoton Wavefunctions

Common approaches to entangled photon pair (or biphoton) generation rely on spontaneous nonlinear parametric processes, where photons from the pump beam of frequency  $\omega_p$  are converted into signal and idler daughter photons having a continuum of frequencies  $\omega_s$  and  $\omega_i$ , but where each detection event satisfies energy conservation, namely  $\omega_s + \omega_i = \omega_p$  for spontaneous parametric down conversion (SPDC) or  $\omega_s + \omega_i = 2\omega_p$  for spontaneous four wave mixing (SFWM). The time and frequency properties of these daughter photons can be represented by the joint spectral intensity (JSI) and joint temporal intensity (JTI), Fig. 9a, b, respectively<sup>169–173</sup>. These correspond to the modulus square of complex amplitudes,  $\psi(\omega_s, \omega_i)$  and  $\psi(t_s, t_i)$ , which are related by a 2D Fourier transform<sup>164,174,175</sup>. Entangled photon joint amplitudes are described by inseparable functions,  $\psi(\omega_s, \omega_i) \neq Y(\omega_s)X(\omega_i)$  and  $\psi(t_s, t_i) \neq y(t_s)x(t_i)$ . This is the key to non-locality, that the processing of one photon of a pair, even though it may be disconnected in space from its twin, always affects the joint biphoton distribution.

In some cases, it is desirable to have entangled photons that are indistinguishable, requiring daughter photons that have as little frequency correlations as possible, yielding a circular JSI<sup>175</sup>. In other cases, high frequency correlations are favoured<sup>176</sup>, like those in Fig. 9a. A key aspect of entangled photon generation is that large, coherent, shapeable, biphoton bandwidth is created from random, spontaneous generation whether the pump is CW or pulsed. Looking at the signal or idler photon alone gives a random, incoherent wavefunction. However, once the time or frequency characteristics of a signal photon are measured, the parameters of its idler twin are known with high precision, leading to a well-defined, coherent phase of the biphoton wavefunction.

As shown by Fig. 9c, d, the spectral and temporal difference-coincidence counts can be found by summing photon counts along the diagonal of the JSI and JTI distributions, respectively. Along the time domain, this gives a probability distribution of the photon arrival times as a function of relative delay, described by the Glauber second order cross-correlation,  $G_{s,i}^{(2)}(t_s - t_i)$ . Since the 1D coincidence probability amplitudes are simpler to measure than their 2D counterparts, most studies have focused on these 1D representations to describe how the biphoton function can be shaped similar to classical (1D) pulses<sup>153,177</sup>. However, it is generally more informative to look at the joint 2D representation since 1D difference-coincidence measurements mix and combine important information from the 2D joint JSI/JTI maps.

The 2D joint representations are particularly useful to visualize phase manipulations. Imposing large spectral phase from GVD on entangled photons gives similar effects as in a classical ultrafast pulse, but now achieved non-locally on the joint probability distribution, see Fig. 9e–j, showing large nonlocal temporal dispersive stretching, nonlocal frequency-to-time mapping, and nonlocal dispersion cancellation, respectively. We note nonlocal quadratic TPM (time-lensing) on entangled biphotons can be similarly understood by simply making the change of variables,  $\omega_s \rightarrow t_s$ , and  $\omega_i \rightarrow t_i$ , (and noting that all JTIs become JSIs and vice versa). In this case, Fig. 9e–j would instead show large nonlocal bandwidth broadening, nonlocal time-to-frequency mapping, and nonlocal bandwidth cancellation<sup>178</sup>. For a more thorough review of joint spectral and temporal distributions and their connections through Fourier processing, as well as further applications of energy redistribution methods via phase manipulations in quantum optics, we address the reader to refs. 171–173, 179–181.

## SPF of Biphoton Wavefunctions

Accurately measuring the JSI of entangled biphotons is critical to characterize the quantum frequency correlations of a source. Reconstructing the JSI is often performed by raster scanning photon pairs using narrowband



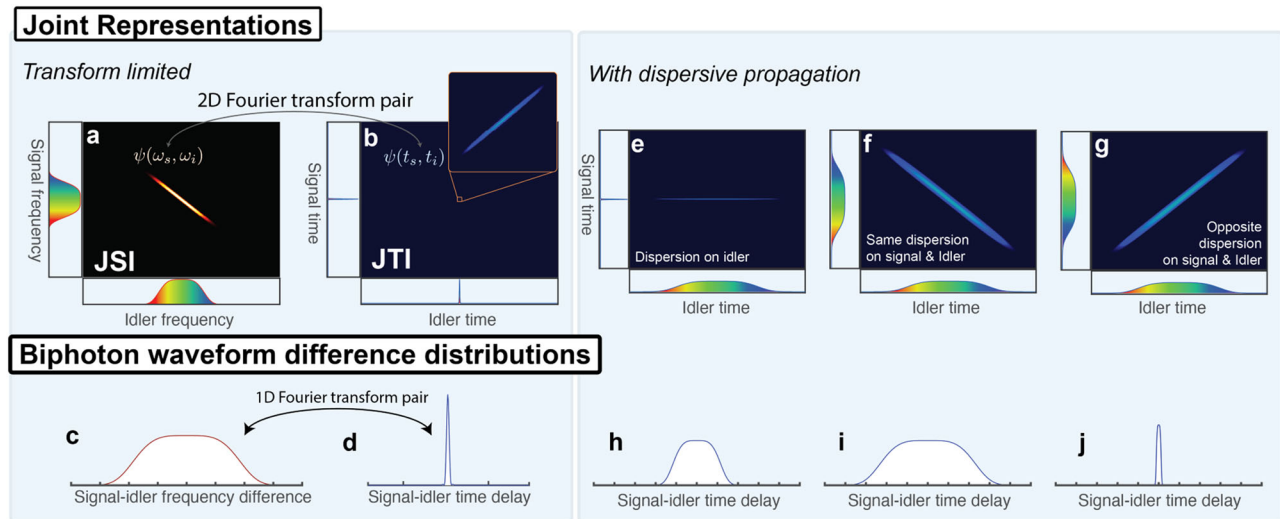


**Fig. 9 | Viewing quantum correlations and the impact of phase manipulations as 2D maps.** **a** An example joint spectral intensity distribution (JSI) of entangled photon pairs and **b** its 2D Fourier transform pair, the joint temporal intensity distribution (JTI). brighter color denotes a higher number of coincidence photon counts; darker denotes a lower number of coincidence counts. These correlations are often measured as histograms of the differences in the **c** frequency or **d** time of arrival, which corresponds to summing along the anti-diagonals in **a** and **b**, respectively. Likewise, these histograms are 1D Fourier transform pairs<sup>169</sup>.

**e** Dispersion will affect the widths in the time domain by stretching the photons and redistributing the energy along the joint time-of-arrival map. In **e**, we show large GVD,  $\phi(\omega_s, \omega_i) = \frac{1}{2}\ddot{\phi}\omega_s^2$  on the signal photons only, **f** large GVD of the same sign on both the signal and idler photons,  $\phi(\omega_s, \omega_i) = \frac{1}{2}\ddot{\phi}\omega_s^2 + \frac{1}{2}\ddot{\phi}\omega_i^2$  (frequency-to-time mapping), and **g** GVD of equal and opposite sign on signal and idler photons,  $\phi(\omega_s, \omega_i) = \frac{1}{2}\ddot{\phi}\omega_s^2 - \frac{1}{2}\ddot{\phi}\omega_i^2$  (nonlocal dispersion cancellation), with their corresponding Glauber second order cross-correlation,  $G_{s,i}^{(2)}(t_s - t_i)$  in **h**, **i**, and **j**, respectively. Figures adapted from<sup>169</sup>.

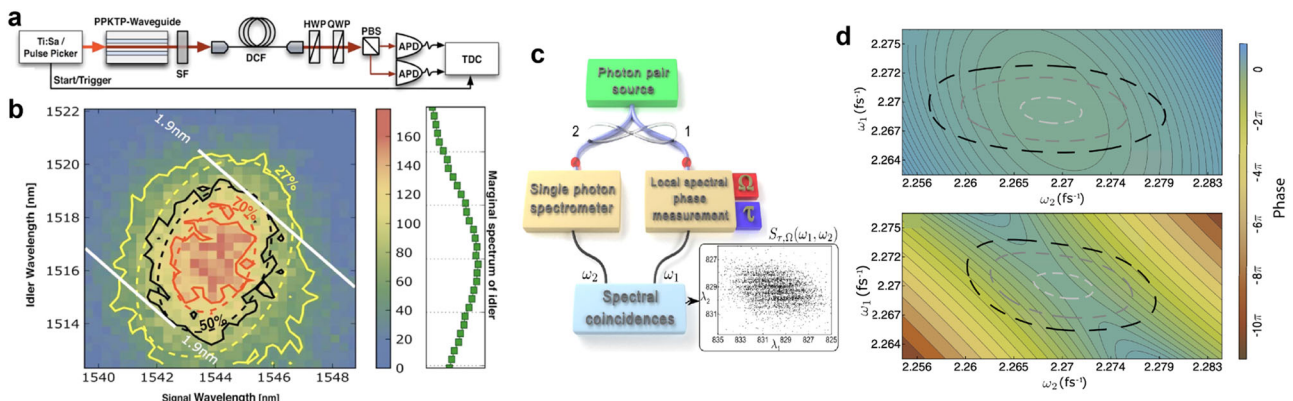


**Fig. 10 | Dispersion-induced frequency-to-time mapping techniques in quantum optics.** **a** Experimental setup for measuring the joint spectral intensity (JSI) of entangled photon pairs by propagation in a dispersion compensating fiber. **b** Resulting JSI, measured in the time domain (axes showing the time-mapped frequencies). Image from<sup>163</sup>. **c** the phase of the joint spectral amplitude can be

obtained by correlating the measurement of the spectrum of one photon from an entangled pair using dispersion-induced frequency-to-time mapping, while the spectral phase of the other photon is measured by electro-optic shearing interferometry. **d** For instance, this allows measuring correlations in the spectral phase resulting from chirped-pulse pumping. Figures adapted from<sup>164</sup>.

spectral filters. Thus, if we consider that a spectral measurement is needed over  $N$  analysis points per spectrum on the signal and idler photons, this means that the JSI is characterized by  $N^2$  points. A simple raster scan using two detectors implies that the signal counts are therefore also reduced by  $N^2$  compared to detection without filtering, significantly increasing the integration time to achieve a similar signal-to-noise performance. This example illustrates the importance of preserving signal counts in quantum processing by avoiding losses and/or techniques that reduce the signal or signal-to-noise ratio.

The frequency-to-time mapping approach, described for classical waves in Chapter 3, provides a clever energy-preserving solution by performing correlated frequency measurements in the time-domain, Fig. 10a, b<sup>163,167</sup>. In this way, all frequencies can be probed simultaneously, limited only by the dead time and resolution of the detectors<sup>167</sup>. The use of low-loss

gratings for the dispersive line allows characterization for wavelengths outside of the telecommunication band where standard dispersive optical fibres have prohibitive losses<sup>166</sup>. Ongoing research aims at improving the frequency resolution, which is limited to  $\sim 10$  s of GHz due to impractically large amounts of dispersion required and insufficient temporal resolution of detectors<sup>182</sup>. Frequency-to-time mapping can also be merged with other signal processing techniques for more intricate measurements, such as intensity interferometry towards measuring the joint spectral mode of photon pairs<sup>183</sup> and spectral shearing interferometry<sup>184,185</sup> for reconstructing the phase of the joint spectral amplitude  $\psi(\omega_s, \omega_i)$ <sup>164</sup>, Fig. 10c, d.

### TPM of Biphoton Wavefunctions

Time-lens techniques have been used extensively for quantum state engineering<sup>186</sup>, temporal resolution enhancement<sup>168,186</sup>, and bandwidth



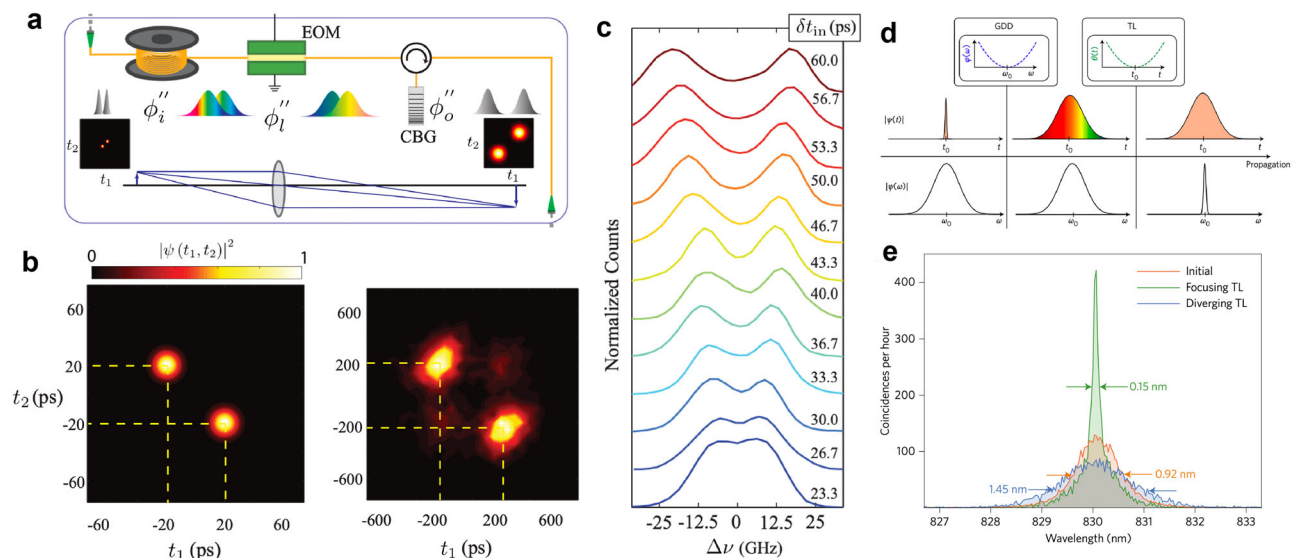


**Fig. 11 | Time-lens based techniques.** **a** Experimental setup for temporal resolution enhancement, allowing for **b** magnification and **c** time-to-frequency mapping of the photon temporal wavefunction. Figures from<sup>168</sup>. **d** Bandwidth compression concept.

**e** Results of a 6-fold bandwidth compression on heralded single-photon wavepackets. Figures adapted from<sup>158</sup>.

compression<sup>158,187</sup>. In the context of quantum state detection, it is often difficult to probe the wavefunction with sufficient temporal resolution using standard detectors. One solution is to employ time-lens magnification prior to detection by using a suitable combination of dispersive lines and a time-lens modulation process<sup>168</sup>, Fig. 11b. Alternatively, this system can be designed to achieve time-to-frequency mapping, enabling the measurement of the biphoton temporal wavefunction in the spectral domain with an increased resolution, Fig. 11c. An important advantage of magnification techniques is that they maintain the energy of the input wavefunction, up to device insertion loss, allowing for both high-resolution and high efficiency detection. However, they are relatively limited in the maximum duration that a waveform can have due to the limited phase excursion of the TPM process. In contrast, temporal gating techniques face similar challenges as raster scan approaches mentioned above for spectral measurements<sup>173,188</sup>.

Another application of time-lens manipulation in quantum optics is for bandwidth compression, using SPF followed by TPM (see Fig. 11d). Using this approach, 6-fold bandwidth compression of heralded single-photon wave packets generated by SPDC was shown as a method towards efficient interfacing between broadband photons and narrowband absorbers, such as quantum memories<sup>158</sup> as shown in Fig. 11e. Ideally, all the photon counts can be concentrated to a much narrower frequency region, boosting the conversion efficiency between different platforms operating at different frequency bandwidths. More recently, this principle was adapted with a temporal analogy to the Fresnel lens to enable a 154-fold compression<sup>160</sup>, confirming the solid potential of this efficient technique for interfacing quantum information processing platforms with very different spectral bandwidths.

Finally, as a last example of work borrowing classical TPM and SPF techniques towards energy preserving quantum wave shaping, we note that noise mitigation based on the TAI principle described in Chapter 4 has also been recently shown to enhance the correlation properties of entangled photons<sup>21</sup>. Here, the single photon waveform is redistributed into a series of peaks, and moreover, the joint temporal distribution of the corresponding biphoton is also distributed into peaks along the 2D joint distribution, JTI. This allows for the post selection of the coherent signal counts contained in the peaks at the expense of the incoherent background noise, enabling improvements in key quantum correlation metrics such as coincidences-to-accidental counts (the quantum equivalent of signal-to-noise ratio).

## Discussion

Though many classical signal processing techniques have already been demonstrated on entangled biphoton waveforms, there still exists numerous opportunities to bring concepts over from the classical signal processing toolbox to the quantum optics regime, particularly since entangled biphoton processing requires manipulation of a 2D, inseparable, joint wavefunction for which there is no classical analogue. However, for entangled biphoton processing techniques to have practical impact for quantum information engineering, they will need to critically address loss and noise. In this chapter, we have focused our brief review on OWER processing techniques based on TPM and SPF since they introduce only passive insertion loss, which can often be engineered to just a few dB. However, it should be also noted that in some quantum channels, even a few dB of loss cannot be tolerated. For instance, in quantum communications, the secret key rate is directly proportional to the channel link loss, which grows exponentially with distance. Since the diminished rates cannot be recovered due to the non-cloning theorem, the reach of quantum communication fiber links is fundamentally limited to a few hundreds of km until efficient quantum repeaters become reality<sup>189</sup>. For example, at a distance of 400 km, only ~10 qubits/s would be detected when considering a GHz clock rate<sup>190</sup>; further losses induced by a processing unit would thus undesirably directly decrease the reachable distance and/or secret key rate. In quantum computing, fault-tolerant architectures have loss thresholds of 50% – implying that the entire processing system must have less than 3 dB loss<sup>191</sup>, representing a stringent bound for future development of photonic hardware. Alternatively, avoiding loss altogether by engineering phase manipulations directly in the biphoton source itself may hold possible solutions<sup>175,192,193</sup>. Likewise, techniques whose signal enhancements exceed the losses they introduce, like high-dimensional cluster state generation<sup>162</sup> and coherent energy redistribution enhancement<sup>21</sup>, may additionally offer pathways to practical wave shaping and processing in quantum networks.

## Integrated Waveguides

Instead of the prepackaged tabletop components employed in the techniques of the previous chapters, it is highly desirable to perform these transformations miniaturized on-chip. Integrated photonics has seen rapid development over recent decades, resulting in the emergence of numerous integrated photonic devices across various platforms. A strong motivator for why integration is so sought after is that certain applications are extremely

constrained in the available weight and footprint, such as in automotive, arial, or satellite applications<sup>16,50</sup>. Along with reducing the physical size of the processing unit, on-chip integration allows for lower latency, more constrained light modes resulting in higher nonlinear coefficients<sup>45,194</sup>, and the potential for wafer scale processing<sup>195</sup>. The last of these allows for the realization of photonic circuits composed of a much higher number of devices for a lower cost than realistically possible using bulk components<sup>195</sup>. A plethora of both active and passive fundamental devices have been successfully integrated on-chip including couplers<sup>22,196,197</sup>, photodetectors<sup>198–200</sup>, light sources<sup>201–203</sup>, modulators<sup>49,204–213</sup>, and integrated dispersive elements<sup>35–37,214–217</sup>. These and integrated TPM and SPF elements are crucial building blocks for fully on-chip OWER signal processing systems.

### Integrated TPM

Recall from Chapter 2 that in an EOPM, the optical signal of interest is given a TPM linearly through an electrical driving signal. One typical implementation of integrated EOPMs involves the use of the plasma dispersion effect on a silicon photonics (SiP) or silicon-on-insulator (SOI) chip, which can readily offer modulation bandwidths greater than 40 GHz and phase modulation efficiencies  $V_{\pi}L < 0.3 \text{ V} \cdot \text{cm}$ <sup>204,207,218</sup>, where  $V_{\pi}$  is the half wave voltage that results in a  $\pi$  phase shift on the incoming light wave. A key advantage of plasma dispersion effects based EOPMs is that they are complementary metal–oxide–semiconductor (CMOS) compatible and can be directly found in the process design kits of commercial foundries. However, a main limitation of EOPM designs on SOI is that they exhibit a severe trade-off between their maximum modulation bandwidth and  $V_{\pi}$ . A lower  $V_{\pi}$  is desired to limit the voltage excursion, i.e., overall energy, of the electrical modulating signal. Recently, various techniques have been investigated to overcome this bottleneck. A promising approach is based on surface plasmon photonics, and this has been shown to enable high-speed EOPM ( $> 65 \text{ GHz}$ ) with a very low halfwave voltage-length product  $V_{\pi}L \approx 1.3 \text{ V} \cdot \text{mm}$ <sup>49</sup>; however, the insertion loss of this device is significantly increased, to  $\sim 12 \text{ dB}$  over a  $29 \mu\text{m}$  long device. Another approach relies on thin film Barium titanate ( $\text{BaTiO}_3$ , BTO) that can provide a large Pockels coefficient, enabling high-speeds ( $> 70 \text{ GHz}$ ) and half wave voltages of  $V_{\pi}L \approx 4.8 \text{ V} \cdot \text{mm}$ <sup>208–210</sup>. More recently, the emerging thin-film lithium-niobate (TFLN) platform has shown extraordinary advantages in the implementation of EOPMs using the Pockels effect. A TFLN EOPM with a length of  $5 \text{ mm}$  has been recently reported that can readily reach a very high-speed modulation  $> 100 \text{ GHz}$  with a  $V_{\pi}$  of only  $1.4 \text{ V}$  (equivalent to  $V_{\pi}L \approx 0.7 \text{ V} \cdot \text{mm}$ ) and a low insertion loss  $< 0.5 \text{ dB}$ <sup>211,212</sup>.

### Integrated SPF

In terms of SPF, the realization of large GVD in an integrated format remains a significant challenge. As an example, the time-lens and TAI-based photonic signal processing schemes discussed above require a GVD equivalent to a SMF hundreds of kilometers long over a wide bandwidth easily exceeding tens or hundreds of GHz. Different solutions have been proposed and demonstrated for the realization of the functionality of a chromatic dispersive line, including arrayed waveguide gratings<sup>215</sup>, lattice filters based on multi-mode interference (MMI) couplers<sup>219</sup>, single<sup>36</sup> or multistage-microring resonators<sup>35</sup> etc. However, most of these techniques suffer from a severe trade-off between useable bandwidth and the amount of GVD that they can provide. An alternative technology is that of the chirped waveguide Bragg grating (CWBG). Similar to a FBG, this device involves a controlled grating corrugation along an optical waveguide in which the grating period or corrugation width is varied along the device length to ensure that different frequencies (or wavelengths) of the propagating light wave are reflected at different locations along the grating, effectively achieving a reflection response with a group delay profile that depends linearly on the wave frequency<sup>216,217</sup>. This technology can offer a remarkable performance, e.g., a measured GVD of  $\sim 1.3 \text{ ps/nm}$  over a  $3 \text{ dB}$  bandwidth of  $\sim 11 \text{ nm}$  for a  $500 \mu\text{m}$  CWBG<sup>18</sup>. As a substantial relative phase excursion necessitates a longer device, the practical implementation of a CWBG is

ultimately restricted by the propagation losses of the material platform (e.g.,  $\sim 1.5 \text{ dB/cm}$  in the case of SOI<sup>220</sup>).

To circumvent this limitation, a CWBG design based on a wide multimode waveguide has been proposed and demonstrated, achieving a  $2.7 \text{ cm}$  long CWBG with a GVD of  $\approx 27.7 \text{ ps/nm}$  and a propagation loss of  $\approx 0.7 \text{ dB/cm}$ <sup>214</sup>. More recently, different low-loss integration platforms have been investigated for the implementation of dispersive devices with a wide operation bandwidth, such as the TFLN platform (low propagation loss  $\approx 3 \text{ dB/m}$ <sup>211,213</sup>) and silicon nitride (SiN) platform (e.g., propagation loss  $\approx 2.4 \text{ dB/m}$ <sup>221</sup>). A demonstration of the remarkable potential offered by these technologies has been reported in Yu et al.<sup>213</sup>, in which an EOPM-based time-lens combined with a highly dispersive device has been used for the generation of ultrafast pulse trains from a continuous-wave (CW) light beam. Modulators (intensity and phase) and the CWBG (GVD  $\approx 1.6 \text{ ps/nm}$ ) have been integrated together to perform this signal processing functionality.

Novel design strategies have been also explored to minimize the nominal length of the integrated SPF devices. In recent work, ultra-compact discrete phase filters have been designed to implement the functionality of a conventional GVD element on an arbitrary optical signal<sup>37</sup>. In contrast to conventional CWBG based implementations, the proposed discretization process ensures that individual spectral phase transitions are bounded within a  $2\pi$  range, exactly as suggested in previous chapters, leading to a far more compact device typically in the mm range. The design flow is represented in Fig. 12. The discretization process involves evaluation of the continuous phase variations of the form Eq. (2.6), at discrete frequency locations  $(\pm k\omega_r)$ ,  $k = 0, 1, 2, \dots$  over the target operation bandwidth<sup>37</sup>, where  $\omega_r$  is the filter's angular frequency resolution. Next, a modulo- $2\pi$  operation of the discrete spectral phase values is performed to ensure that the resultant phase profile is bounded within the  $0$  to  $2\pi$  range, shown in Fig. 12b for the case of a  $31.12\text{-km}$  fibre-optic link. This  $4.1 \text{ mm}$  long discrete phase filter effectively emulates the continuous phase variation of the target dispersive line as long as this phase profile remains approximately constant over the filter's frequency resolution ( $\nu_r = 10 \text{ GHz}$  in this case). Supported by mathematical derivations and system-level simulations, it has been shown that the maximum group-delay excursion (i.e., the product of GVD and operation bandwidth) that can be emulated with the proposed discrete SPF approach is inversely proportional to the frequency resolution  $\nu_r$  of the filter. For example, the GVD equivalent to  $70.56\text{-km}$  SMF can be achieved when  $\nu_r = 2 \text{ GHz}$ <sup>222,223</sup>.

### Discussion

GVD compensation of telecom data signals with speeds up to  $32 \text{ Gbps}$  has been successfully demonstrated over a  $31.12\text{-km}$  fibre optic link, utilizing mm-long WBG-based discrete phase filters in the SOI platform. The reported devices provide at least five times reduction in length compared to a CWBG. A schematic of the designed on-chip layout is displayed in Fig. 12e. The SOI chip in this case was fabricated using electron beam lithography and inductively coupled reactive ion etching. Experimental verification of the device's potential for GVD compensation of telecom data signals was demonstrated for both non-return-to-zero on-off keying (NRZ-OOK) and four level pulse amplitude modulation (PAM4) formats. The respective eye diagrams are presented in Fig. 13a, b.

We envision that highly dispersive lines offering the required GVD and bandwidth performance for demanding high-speed OWER signal processing applications could be realized in integrated formats through a combination of novel and more compact design strategies, such as the discrete SPF approach discussed above, and lower-loss photonic integration platforms, such as TFLN and SiN. This would enable the integration of high-speed OWER signal processing systems, such as those described in the previous chapters, on a single chip through co-integration of SPF elements such as highly dispersive lines and TPM elements such as EOPMs, all with the required control electronics.

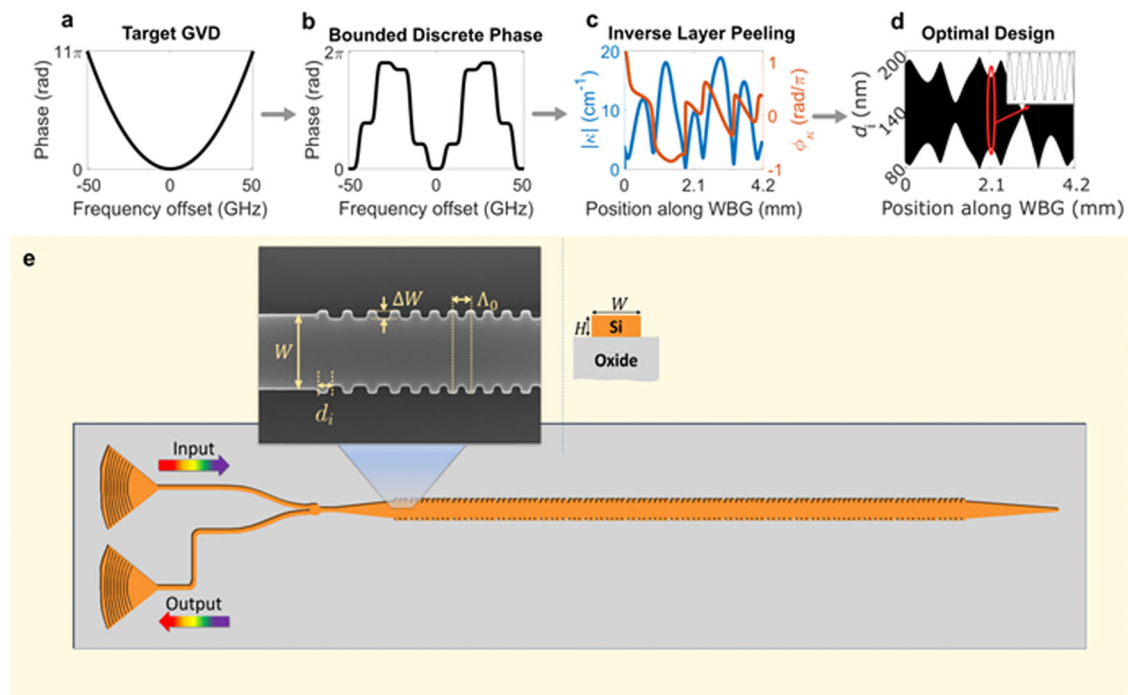


**Fig. 12 | Design flow of the proposed discrete phase filtering based dispersive element.** **a** A continuous quadratic spectral phase variation of a 31.12-km SMF. **b** The resultant discretized and bounded within  $[0, 2\pi)$  phase levels with frequency resolution  $\nu_r = 10$  GHz. Note, the amplitude response of the filter is assumed to be constant over the operation bandwidth (i.e., all-pass response)<sup>37</sup>. The target spectral transfer function is implemented using a waveguide Bragg grating (WBG) structure. **c** The complex coupling coefficient profile ( $\kappa = |\kappa(z)| \exp(j\phi_\kappa(z))$ ) of the WBG; magnitude  $|\kappa(z)|$  on the left and phase  $\phi_\kappa(z)$  on the right. An inverse layer peeling algorithm is employed to calculate the complex coupling coefficient ( $\kappa$ ) profile,  $\kappa(z) = |\kappa(z)| \exp(j\phi_\kappa(z))$  i.e., the strength and phase of the coupling induced between the forward and backward propagating modes per unit length along the WBG, that is required to achieve the target spectral response<sup>222</sup>. A phase modulated apodization technique is employed to practically implement the target coupling

coefficient<sup>223</sup>. **d** A phase modulated grating based apodization is employed to physically realize the target coupling coefficient by modulating the distances ( $d_i$ ) between adjacent corrugations while keeping the corrugation width ( $\Delta W$ ) constant.  $\Lambda_0$  is the nominal grating period.  $H$  and  $W$  represent the waveguide height and width, respectively. **e** Schematic of the on-chip layout utilized for coupling light in and out of the WBG-based phase filter. The zoomed-in view shows the SEM image of one of the fabricated WBGs. The cross-sectional schematic of the fully etched silicon waveguide on top of the buried oxide is also shown. A Y-splitter collects the reflected signal from the WBG. A 20- $\mu\text{m}$  linear adiabatic taper connects the input single-mode waveguide ( $W = 0.5 \mu\text{m}$ ) with the 2- $\mu\text{m}$  wide multimode waveguide. The transmitted signal from the WBG is terminated using a taper. Figures adapted from<sup>37,222,223</sup>.

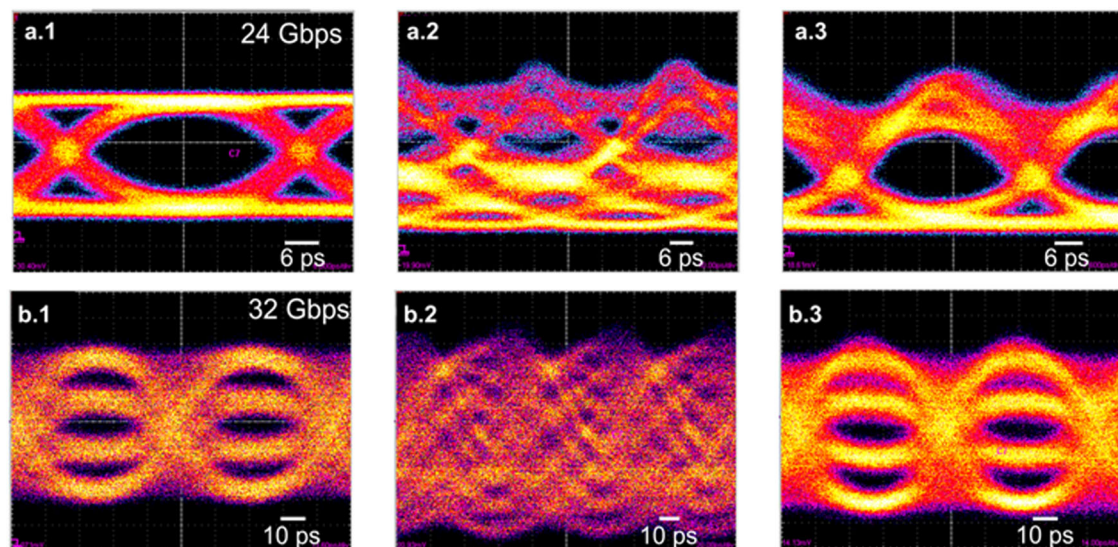


**Fig. 13 | Measurements related to GVD compensation of NRZ-OOK and PAM4 data signals after propagation through a 31.12 km section of SMF using the WBG-based phase filter.** The top row corresponds to eye diagrams of **a.1** the input

24-Gbps NRZ signal, **a.2** after dispersive propagation, **a.3** and after reflection from the WBG. The bottom row depicts the **b.1** input, **b.2** dispersed, and **b.3** WBG output eye diagrams for a 16-GBd (32 Gbps) PAM4 signal. Figures adapted from<sup>37</sup>.



## Conclusion

An overview of several optical signal processing functionalities based on linear optical wave energy redistribution (OWER) methods has been presented. Using spectral phase filtering (SPF) and temporal phase modulation (TPM), ideally preserving the total energy of the signal of interest, a wide variety of mathematical transformations can be implemented. Specifically, we have discussed real-time and gapless spectral analysis, passive denoising and amplification, passive logic operations, and quantum optics signal processing, as well as recent advances in integration on-chip. These techniques are relevant to any application involving information encoded on an optical wave, naturally or artificially, including when an RF or microwave signal is upconverted to an optical carrier. This includes optical telecommunications, radar, sensing, metrology, astronomy, biomedical imaging, and more. The continually increasing demand for faster signal processing over higher bandwidths necessitates the inclusion and integration of optical processing technologies. Energy preserving OWER methods provide competitive functionalities which will continue to improve and generalize.

## Data Availability

No datasets were generated or analysed during the current study.

Received: 4 July 2024; Accepted: 2 February 2025;

Published online: 03 April 2025

## References

- Agrawal, G. P. *Optics in Our Time* 177–199 (Springer International Publishing, 2016).
- Moore, G. E. Cramming more components onto integrated circuits. *Electron. Mag.* **38**, 114–117 (1965).
- Shalf, J. The future of computing beyond Moore's Law. *Philos. Trans. R. Soc. A* **378**, 20190061 (2020).
- Markov, I. L. Limits on fundamental limits to computation. *Nature* **512**, 147–154 (2014).
- Radosavljevic, M. & Kavalieros, J. Taking Moore's Law to new heights: when transistors can't get any smaller, the only direction is up. In *IEEE Spectrum* (IEEE, 2022).
- Smith, P. W. Photonic switching devices: recent advances. In *International Conference on Quantum Electronics ThH1* (Optica Publishing Group, 1988).
- Agrawal, G. P. & Dutta, N. K. *Semiconductor Lasers* 487–529 (Springer International Publishing, 1993).
- Lin, L. Y. & Goldstein, E. L. Roles of MEMS optical switches in fiber optic networks: what and when. In *Active and Passive Optical Components for WDM Communications III* 85–94 (SPIE, 2003).
- Macleod, H. A. Challenges in the design and production of narrow-band filters for optical fiber telecommunications. In *Proc. Optical and Infrared Thin Films* 46–57 (SPIE, 2000).
- Pérez, D. et al. Multipurpose silicon photonics signal processor core. *Nat. Commun.* **8**, 636 (2017).
- Bland-Hawthorn, J. & Kern, P. Astrophotonics: a new era for astronomical instruments. *Opt. Express* **17**, 1880–1884 (2009).
- Ntziachristos, V., Ripoll, J., Wang, L. V. & Weissleder, R. Looking and listening to light: the evolution of whole-body photonic imaging. *Nat. Biotechnol.* **23**, 313–320 (2005).
- Lee, B. H., Min, E. J. & Kim, Y. H. Fiber-based optical coherence tomography for biomedical imaging, sensing, and precision measurements. *Opt. Fiber Technol.* **19**, 729–740 (2013).
- Li, Y. & Ibanez-Guzman, J. Lidar for Autonomous Driving: The Principles, Challenges, and Trends for Automotive Lidar and Perception Systems. *IEEE Signal Process. Mag.* **37**, 50–61 (2020).
- Saleh, B. & Teich, M. *Fundamentals of Photonics* 3rd edn (Wiley, 2019).
- Marpaung, D., Yao, J. & Capmany, J. Integrated microwave photonics. *Nat. Photon* **13**, 80–90 (2019).
- Ghelfi, P. et al. A fully photonics-based coherent radar system. *Nature* **507**, 341–345 (2014).
- Pan, S. & Zhang, Y. Microwave photonic radars. *J. Lightwave Technol.* **38**, 5450–5484 (2020).
- Crockett, B., Romero Cortés, L., Konatham, S. R. & Azaña, J. Full recovery of ultrafast waveforms lost under noise. *Nat. Commun.* **12**, 2402 (2021).
- Shih, Y. *An Introduction to Quantum Optics: Photon and Biphoton Physics* (CRC Press, 2014).
- Crockett, B. et al. Enhancing the quantum correlation of biphotons via coherent energy redistribution. In *2023 Optical Fiber Communications Conference and Exhibition* 1–3 (IEEE, 2023).
- Thomson, D. et al. Roadmap on silicon photonics. *J. Opt.* **18**, 073003 (2016).
- Weiner, A. M. *Ultrafast Optics* (Wiley, 2011).
- Oppenheim, A. V., Willsky, A. S. & Nawab, S. H. *Signals & Systems* (Pearson Education India, 1997).
- Madsen, C. K. & Zhao, J. H. *Optical Filter Design and Analysis: A Signal Processing Approach* (Wiley, 1999).
- Agrawal, G. *Nonlinear Fiber Optics* (Academic, 2012).
- Kolner, B. H. Space-time duality and the theory of temporal imaging. *IEEE J. Quantum Electron.* **30**, 1951–1963 (1994).
- Hecht, E. *Optics* (Pearson Education, 2017).
- Salem, R., Foster, M. A. & Gaeta, A. L. Application of space-time duality to ultrahigh-speed optical signal processing. *Adv. Opt. Photon.* **5**, 274–317 (2013).
- Cohen, L. *Time-Frequency Analysis* (Prentice Hall, 1995).
- Weiner, A. M. Ultrafast optical pulse shaping: a tutorial review. *Opt. Commun.* **284**, 3669–3692 (2011).
- XSoptix. WaveShaper® series A family of programmable optical processors. [https://www.xsoptix.com/data/finisar/ds\\_fnstr\\_instr\\_waveshaper\\_A\\_series\\_product\\_guide.pdf](https://www.xsoptix.com/data/finisar/ds_fnstr_instr_waveshaper_A_series_product_guide.pdf) (2021).
- Ouellette, F. All-fiber filter for efficient dispersion compensation. *Opt. Lett.* **16**, 303–305 (1991).
- Kashyap, R. *Fiber Bragg Gratings* (Academic, 2010).
- Madsen, C. K. et al. Multistage dispersion compensator using ring resonators. *Opt. Lett.* **24**, 1555–1557 (1999).
- Ong, K. Y. K., Chen, G. F. R., Xing, P., Gao, H. & Tan, D. T. H. Dispersion compensation of high-speed data using an integrated silicon nitride ring resonator. *Opt. Express* **30**, 13959–13967 (2022).
- Kaushal, S., Roberge, A., Kashyap, R. & Azaña, J. Ultra-compact silicon photonics highly dispersive elements for low-latency signal processing. *Opt. Express* **31**, 3467–3478 (2023).
- Cincotti, G. et al. Enhanced optical communications through joint time-frequency multiplexing strategies. *J. Lightwave Technol.* **38**, 346–351 (2020).
- Campanella, C. E., Cuccovillo, A., Campanella, C., Yurt, A. & Passaro, V. M. N. Fibre Bragg grating based strain sensors: review of technology and applications. *Sensors* **18**, 3115 (2018).
- Tosi, D. Review of chirped fiber Bragg Grating (CFBG) fiber-optic sensors and their applications. *Sensors* **18**, 2147 (2018).
- Gagné, M., Loranger, S., Lapointe, J. & Kashyap, R. Fabrication of high quality, ultra-long fiber Bragg gratings: up to 2 million periods in phase. *Opt. Express* **22**, 387 (2014).
- AB Proximion. DCM-HDC\_Datasheet.pdf. [https://www.proximion.com/hubs/bu-pr/datasheet/dispersion-compensation/DCM-HDC\\_Datasheet.pdf](https://www.proximion.com/hubs/bu-pr/datasheet/dispersion-compensation/DCM-HDC_Datasheet.pdf) (2024).
- Boyd, R. W. *Nonlinear Optics* (Academic, 2008).
- Howe, J. et al. Ultrafast optical signal processing based upon space-time dualities. *J. Lightwave Technol.* **24**, 2649 (2006).
- Chia, X. X. et al. Low-power four-wave mixing in deuterated silicon-rich nitride ring resonators. *J. Lightwave Technol.* **41**, 3115–3130 (2023).



46. Klein, A., Shahal, S., Masri, G., Duadi, H. & Fridman, M. Four wave mixing-based time lens for orthogonal polarized input signals. *IEEE Photonics J.* **9**, 1–7 (2017).
47. Salem, R. et al. Optical time lens based on four-wave mixing on a silicon chip. *Opt. Lett.* **33**, 1047 (2008).
48. Huh, J. & Azana, J. All-optical reconfigurable signal processing based on cross phase modulation time lensing. *IEEE Photon. Technol. Lett.* **29**, 826–829 (2017).
49. Melikyan, A. et al. High-speed plasmonic phase modulators. *Nat. Photon* **8**, 229–233 (2014).
50. Zhu, D. et al. Integrated photonics on thin-film lithium niobate. *Adv. Opt. Photon.* **13**, 242 (2021).
51. Goodman, J. W. *Introduction to Fourier Optics* (W.H. Freeman, 2017).
52. Krakowski, M., Kwaśny, A. & Soboń, G. Amplification of femtosecond pulses with Al-assisted spectral phase modulation. *Opt. Contin.* **3**, 449 (2024).
53. Thomas, S., Malacarne, A., Fresi, F., Poti, L. & Azana, J. Fiber-based programmable picosecond optical pulse shaper. *J. Lightwave Technol.* **28**, 1832–1843 (2010).
54. Lin, X. et al. All-optical machine learning using diffractive deep neural networks. *Science* **361**, 1004–1008 (2018).
55. Lin, Z., Sun, S., Azaña, J., Li, W. & Li, M. High-speed serial deep learning through temporal optical neurons. *Opt. Express* **29**, 19392 (2021).
56. Xu, X. et al. 11 TOPS photonic convolutional accelerator for optical neural networks. *Nature* **589**, 44–51 (2021).
57. Stoica, P. G., Moses, R., Stoica, P. & Moses, R. L. *Spectral Analysis of Signals* (Prentice Hall, 2005).
58. Majid, W. A. et al. A bright fast radio burst from FRB 20200120E with sub-100 nanosecond structure. *ApJL* **919**, L6 (2021).
59. Sharma, P., Sarma, K. K. & Mastorakis, N. E. Artificial intelligence aided electronic warfare systems- recent trends and evolving applications. *IEEE Access* **8**, 224761–224780 (2020).
60. Zou, X. et al. Photonics for microwave measurements. *Laser Photonics Rev.* **10**, 711–734 (2016).
61. Zuo, P., Ma, D. & Chen, Y. Short-time Fourier transform based on stimulated brillouin scattering. *J. Lightwave Technol.* **40**, 5052–5061 (2022).
62. Bui, L. A. et al. Instantaneous frequency measurement system using optical mixing in highly nonlinear fiber. *Opt. Express* **17**, 22983–22991 (2009).
63. Guillet De Chatellus, H., Cortés, L. R. & Azaña, J. Optical real-time Fourier transformation with kilohertz resolutions. *Optica* **3**, 1 (2016).
64. Tainta, S., Erro, M. J., Garde, M. J. & Muriel, M. A. Temporal self-imaging effect for periodically modulated trains of pulses. *Opt. Express* **22**, 15251 (2014).
65. Azana, J. & Muriel, M. A. Real-time optical spectrum analysis based on the time-space duality in chirped fiber gratings. *IEEE J. Quantum Electron.* **36**, 517–526 (2000).
66. Mahjoubfar, A. et al. Time stretch and its applications. *Nat. Photon* **11**, 341–351 (2017).
67. Torres-Company, V., Leaird, D. E. & Weiner, A. M. Dispersion requirements in coherent frequency-to-time mapping. *Opt. Express* **19**, 24718–24729 (2011).
68. Li, F. & Azaña, J. Simplified system configuration for real-time Fourier transformation of optical pulses in amplitude and phase. *Opt. Commun.* **274**, 59–65 (2007).
69. Wu, Z., Lei, L., Dong, J., Hou, J. & Zhang, X. Reconfigurable temporal Fourier transformation and temporal imaging. *J. Lightwave Technol.* **32**, 4565–4570 (2014).
70. Berger, N., Levit, B., Atkins, S. & Fischer, B. Time-lens-based spectral analysis of optical pulses by electrooptic phase modulation. *Electron. Lett.* **36**, 1 (2000).
71. Azaña, J. Time-to-frequency conversion using a single time lens. *Opt. Commun.* **217**, 205–209 (2003).
72. Romero Cortés, L., Onori, D., Guillet De Chatellus, H., Burla, M. & Azaña, J. Towards on-chip photonic-assisted radio-frequency spectral measurement and monitoring. *Optica* **7**, 434 (2020).
73. Saperstein, R. E., Panasenko, D. & Fainman, Y. Demonstration of a microwave spectrum analyzer based on time-domain optical processing in fiber. *Opt. Lett.* **29**, 501 (2004).
74. Gadringer, M. E. et al. Radar target stimulation for automotive applications. *IET Radar, Sonar Navigation* **12**, 1096–1103 (2018).
75. Bell, R. *Introductory Fourier Transform Spectroscopy* (Elsevier, 2012).
76. Sun, H., Nallanathan, A., Wang, C.-X. & Chen, Y. Wideband spectrum sensing for cognitive radio networks: a survey. *IEEE Wirel. Commun.* **20**, 74–81 (2013).
77. Goda, K. & Jalali, B. Dispersive Fourier transformation for fast continuous single-shot measurements. *Nat. Photon* **7**, 102–112 (2013).
78. Liu, Q. & Fok, M. P. Ultrafast and wideband microwave photonic frequency-hopping systems: a review. *Appl. Sci.* **10**, 521 (2020).
79. Konatham, S. R. et al. Photonics-based real-time spectrogram analysis of broadband waveforms. *J. Lightwave Technol.* **38**, 5356–5367 (2020).
80. Konatham, S. R. et al. Real-time gap-free dynamic waveform spectral analysis with nanosecond resolutions through analog signal processing. *Nat. Commun.* **11**, 3309 (2020).
81. Xie, X., Li, J., Yin, F., Xu, K. & Dai, Y. STFT based on bandwidth-scaled microwave photonics. *J. Lightwave Technol.* **39**, 1680–1687 (2021).
82. Crockett, B., Rowe, C. & Azaña, J. Capturing ultra-broadband complex-fields of arbitrary duration using a real-time spectrogram. *APL Photonics* **8**, 066108 (2023).
83. Rowe, C. M. L., Crockett, B. & Azana, J. Real-time gapless analog time frequency analysis for bandwidths above 20 GHz with nanosecond resolution. In *2021 European Conference on Optical Communication* 1–4 (IEEE, 2021).
84. Zhu, X., Crockett, B., Rowe, C. M. L. & Azaña, J. Photonics-enabled nanosecond scale real-time spectral analysis with 92-GHz bandwidth and MHz resolution. In *Optical Fiber Communication Conference M1J.5* (Optica, 2023).
85. Zhu, X., Crockett, B., Rowe, C. M. L. & Azaña, J. Photonics-based real-time spectral analysis over 40-GHz bandwidth with fine frequency resolution. In *IEEE Research and Applications of Photonics in Defense Conference* 1–2 (IEEE, 2023).
86. Azaña, J., Zhu, X., Rowe, C. & Crockett, B. Optical time-mapped spectrograms (II): fractional Talbot designs. *J. Lightwave Technol.* **41**, 5284–5295 (2023).
87. Crockett, B., Romero Cortés, L., Maram, R. & Azaña, J. Optical signal denoising through temporal passive amplification. *Optica* **9**, 130 (2022).
88. Fernández, M. P. et al. Nonlinear time-lens with improved power efficiency through a discrete multilevel pump. *Opt. Lett.* **45**, 3557 (2020).
89. Rowe, C. M. L., Crockett, B., Zhu, X. & Azaña, J. Versatile photonics spectrograms for ultrafast real-time broadband microwave signal analysis. In *IEEE Transactions on Microwave Theory and Techniques* (IEEE, 2024).
90. Zhu, X., Crockett, B., Rowe, C.M.L., Sun, H. & Azaña, J. Agile manipulation of the time-frequency distribution of high-speed electromagnetic waves. *Nat. Commun.* **15**, 8942 (2024).
91. Sun, Y., Wang, S., Chen, J. & Wu, G. Fast and large-range frequency hopping receiving based on simultaneous photonic filtering and digitizing. *Opt. Lett.* **46**, 749–752 (2021).
92. Liu, C. et al. Investigation of signal-to-noise ratio performance of microwave photonic links enhanced by optical injection locking and

- channelized spectrum stitching. *Opt. Express* **30**, 19731–19744 (2022).
93. Qiang, W. et al. Mitigation of amplified spontaneous emission noise for an all-fiber coaxial aerosol lidar with different single-photon detectors. *Opt. Express* **30**, 23187–23197 (2022).
  94. Bi, Y. et al. ASE noise mitigation with digital frequency offset loading for discrete spectrum nonlinear frequency division multiplexing systems. *Opt. Lett.* **48**, 5707–5710 (2023).
  95. Solli, D. R., Chou, J. & Jalali, B. Amplified wavelength–time transformation for real-time spectroscopy. *Nat. Photon* **2**, 48–51 (2008).
  96. Bottacchi, S. *Noise and Signal Interference in Optical Fiber Transmission Systems: An Optimum Design Approach* (Wiley, 2008).
  97. Desurvire, E. *Erbium-Doped Fiber Amplifiers: Principles and Applications* (Wiley, 2002).
  98. Hansryd, J., Andrekson, P. A., Westlund, M., Li, J. & Hedekvist, P.-O. Fiber-based optical parametric amplifiers and their applications. *IEEE J. Sel. Top. Quantum Electron.* **8**, 506–520 (2002).
  99. Romero Cortés, L., Maram, R., Guillet de Chatellus, H. & Azaña, J. Arbitrary energy-preserving control of optical pulse trains and frequency combs through generalized Talbot effects. *Laser Photonics Rev.* **13**, 1900176 (2019).
  100. Cundiff, S. T. & Weiner, A. M. Optical arbitrary waveform generation. *Nat. Photon* **4**, 760–766 (2010).
  101. Torres-Company, V. & Weiner, A. M. Optical frequency comb technology for ultra-broadband radio-frequency photonics. *Laser Photonics Rev.* **8**, 368–393 (2014).
  102. Diddams, S. A., Hollberg, L. & Mbele, V. Molecular fingerprinting with the resolved modes of a femtosecond laser frequency comb. *Nature* **445**, 627–630 (2007).
  103. Coddington, I., Newbury, N. & Swann, W. Dual-comb spectroscopy. *Optica* **3**, 414–426 (2016).
  104. Picqué, N. & Hänsch, T. W. Frequency comb spectroscopy. *Nat. Photon* **13**, 146–157 (2019).
  105. McGrew, W. F. et al. Towards the optical second: verifying optical clocks at the SI limit. *Opt., Opt.* **6**, 448–454 (2019).
  106. Steinmetz, T. et al. Laser frequency combs for astronomical observations. *Science* **321**, 1335–1337 (2008).
  107. Roztock, P. & Morandotti, R. Astrocombs for extreme-precision spectroscopy. *Nat. Astron.* **3**, 135–136 (2019).
  108. Pfeifle, J. et al. Coherent terabit communications with microresonator Kerr frequency combs. *Nat. Photon* **8**, 375–380 (2014).
  109. Marin-Palomo, P. et al. Microresonator-based solitons for massively parallel coherent optical communications. *Nature* **546**, 274–279 (2017).
  110. Kues, M. et al. On-chip generation of high-dimensional entangled quantum states and their coherent control. *Nature* **546**, 622–626 (2017).
  111. Jansson, T. & Jansson, J. Temporal self-imaging effect in single-mode fibers. *J. Opt. Soc. Am.* **71**, 1373–1376 (1981).
  112. Andrekson, P. A. Linear propagation of optical picosecond pulse trains over oceanic distances. *Opt. Lett.* **18**, 1621–1623 (1993).
  113. Arahira, S., Kutsuzawa, S., Matsui, Y., Kunitatsu, D. & Ogawa, Y. Repetition-frequency multiplication of mode-locked pulses using fiber dispersion. *J. Lightwave Technol.* **16**, 405–410 (1998).
  114. Shake, I., Takara, H., Kawanishi, S. & Saruwatari, M. High-repetition-rate optical pulse generation by using chirped optical pulses. *Electron. Lett.* **34**, 792–793 (1998).
  115. Azaña, J. & Muriel, M. A. Technique for multiplying the repetition rates of periodic trains of pulses by means of a temporal self-imaging effect in chirped fiber gratings. *Opt. Lett.* **24**, 1672–1674 (1999).
  116. Azana, J. & Muriel, M. A. Temporal self-imaging effects: theory and application for multiplying pulse repetition rates. *IEEE J. Sel. Top. Quantum Electron.* **7**, 728–744 (2001).
  117. Longhi, S. et al. 40-GHz pulse-train generation at 1.5  $\mu\text{m}$  with a chirped fiber grating as a frequency multiplier. *Opt. Lett.* **25**, 1481–1483 (2000).
  118. Cortés, L. R., Guillet de Chatellus, H. & Azaña, J. On the generality of the Talbot condition for inducing self-imaging effects on periodic objects. *Opt. Lett.* **41**, 340 (2016).
  119. Maram, R. et al. Frequency-domain ultrafast passive logic: NOT and XNOR gates. *Nat. Commun.* **11**, 5839 (2020).
  120. Maram, R., Cortés, L. R. & Azaña, J. Programmable fiber-optics pulse repetition-rate multiplier. *J. Lightwave Technol.* **34**, 448–455 (2016).
  121. Azaña, J. Spectral Talbot phenomena of frequency combs induced by cross-phase modulation in optical fibers. *Opt. Lett.* **30**, 227–229 (2005).
  122. Caraquitena, J., Beltrán, M., Llorente, R., Martí, J. & Muriel, M. A. Spectral self-imaging effect by time-domain multilevel phase modulation of a periodic pulse train. *Opt. Lett.* **36**, 858–860 (2011).
  123. Caraquitena, J., Jiang, Z., Leaird, D. E. & Weiner, A. M. Tunable pulse repetition-rate multiplication using phase-only line-by-line pulse shaping. *Opt. Lett.* **32**, 716–718 (2007).
  124. Zhang, Y., Zhang, H. & Shu, C. Tunable optical frequency comb with hundred-GHz spacings generated on a silicon waveguide. *Opt. Lett.* **47**, 2987–2990 (2022).
  125. Li, Z. et al. Four-wave mixing based spectral Talbot amplifier for programmable purification of optical frequency combs. *APL Photonics* **9**, 036101 (2024).
  126. IEEE Xplore. A tutorial on microwave photonic filters. IEEE Journals & Magazine. <https://ieeexplore.ieee.org/document/1589051>.
  127. Pelusi, M., Inoue, T. & Namiki, S. Enhanced carrier to noise ratio by Brillouin amplification for optical communications. *J. Lightwave Technol.* **38**, 319–331 (2020).
  128. Marpaung, D. et al. Low-power, chip-based stimulated Brillouin scattering microwave photonic filter with ultrahigh selectivity. *Optica* **2**, 76–83 (2015).
  129. Choudhary, A., Liu, Y., Marpaung, D. & Eggleton, B. J. On-chip Brillouin filtering of RF and optical signals. *IEEE J. Sel. Top. Quant.* **24**, 76000211 (2018).
  130. Vasilyev, M. Matched filtering of ultrashort pulses. *Science* **350**, 1314–1315 (2015).
  131. Wang, J. et al. In-band noise filtering via spatio-spectral coupling. *Laser Photonics Rev.* **12**, 1700316 (2018).
  132. Mesgarani, N. & Shamma, S. Denoising in the domain of spectrotemporal modulations. *J. Audio Speech Music Proc.* **2007**, 1–8 (2007).
  133. Hao, L. et al. Denoising method based on spectral subtraction in time-frequency domain. *Adv. Civ. Eng.* **2021**, 6621596 (2021).
  134. Balster, E. J., Zheng, Y. F. & Ewing, R. L. Combined spatial and temporal domain wavelet shrinkage algorithm for video denoising. *IEEE Trans. Circuits Syst. Video Technol.* **16**, 220–230 (2006).
  135. Maram, R., Van Howe, J., Li, M. & Azaña, J. Noiseless intensity amplification of repetitive signals by coherent addition using the temporal Talbot effect. *Nat. Commun.* **5**, 5163 (2014).
  136. Romero Cortés, L., Maram, R., Guillet de Chatellus, H. & Azaña, J. Subnoise detection and passive amplification of frequency combs through customized coherent spectral energy redistribution. *Phys. Rev. Appl.* **9**, 064017 (2018).
  137. Zhu, G., Van Howe, J., Durst, M., Warren, Z. & Xu, C. Simultaneous spatial and temporal focusing of femtosecond pulses. *Opt. Express* **13**, 2153–2159 (2005).
  138. Fernández-Pousa, C. R. On the structure of quadratic Gauss sums in the Talbot effect. *J. Opt. Soc. Am. A* **34**, 732 (2017).
  139. Nuño, J., Finot, C. & Fatome, J. Linear sampling and magnification technique based on phase modulators and dispersive elements: the temporal lenticular lens. *Optical Fiber Technol.* **36**, 125–129 (2017).

140. Fatome, J., Pitois, S. & Millot, G. Influence of third-order dispersion on the temporal Talbot effect. *Opt. Commun.* **234**, 29–34 (2004).
141. Zhao, Y. et al. Repetition rate multiplication control of micro-combs assisted by perfect temporal Talbot effect. *APL Photonics* **5**, 046102 (2020).
142. Fernández, M. P. et al. An ultra-fast temporal Talbot array illuminator. *J. Lightwave Technol.* **41**, 4725–4733 (2023).
143. Li, Z. et al. All-optical purification of arbitrary spectral waveforms via cross-phase modulation based spectral Talbot amplifier. In *CLEO 2023 STh3N.2* (Optica Publishing Group, 2023).
144. Driouche, Y., Mwamsojo, N., Hamdi, R. & Benkelfat, B.-E. Programmable all-optical talbot amplifier using XPM-based discrete multilevel time-lens. In *CLEO 2023 STh3N.1* (Optica Publishing Group, 2023).
145. Fernandez, M. P. et al. All-optical parametric-assisted oversampling and decimation for signal denoising amplification. *Laser Photonics Rev.* **17**, 2200711 (2023).
146. Fernández, M. P. et al. Combined parametric and denoising passive amplification by FWM-based oversampling and Talbot-based decimation. In *Optical Fiber Communication Conference M1J.7* (Optica Publishing Group, 2023).
147. Pudo, D., Depa, M. & Chen, L. R. Single and multiwavelength all-optical clock recovery in single-mode fiber using the temporal Talbot effect. *J. Lightwave Technol.* **25**, 2898–2903 (2007).
148. Maram, R., Cortés, L. R. & Azaña, J. Sub-harmonic periodic pulse train recovery from aperiodic optical pulse sequences through dispersion-induced temporal self-imaging. *Opt. Express* **23**, 3602–3613 (2015).
149. Maram, R., Kong, D., Galili, M., Oxenløwe, L. K. & Azaña, J. 640 Gbit/s return-to-zero to non-return-to-zero format conversion based on optical linear spectral phase filtering. *Opt. Lett.* **41**, 64–67 (2016).
150. Kaushal, S. et al. All-fibre phase filters with 1-GHz resolution for high-speed passive optical logic processing. *Nat. Commun.* **14**, 1808 (2023).
151. Tucker, R. S. The role of optics in computing. *Nat. Photon* **4**, 405–405 (2010).
152. Goodarzi, M., Fernandez, M. P., Zhu, X. & Azaña, J. Narrowband Noise Filtering Of Arbitrary Waveforms By Reversible In-fiber Temporal Talbot sampling. In *Optical Fiber Communication Conference Th3F.7* (Optica Publishing Group, 2024).
153. Pe'er, A., Dayan, B., Friesem, A. A. & Silberberg, Y. Temporal shaping of entangled photons. *Phys. Rev. Lett.* **94**, 073601 (2005).
154. Wootters, W. K. & Zurek, W. H. A single quantum cannot be cloned. *Nature* **299**, 802–803 (1982).
155. Capmany, J. & Fernández-Pousa, C. R. Quantum modelling of electro-optic modulators. *Laser Photonics Rev.* **5**, 750–772 (2011).
156. Ashby, J. et al. Temporal mode transformations by sequential time and frequency phase modulation for applications in quantum information science. *Opt. Express* **28**, 38376–38389 (2020).
157. Bernhard, C., Bessire, B., Feurer, T. & Stefanov, A. Shaping frequency-entangled qubits. *Phys. Rev. A* **88**, 032322 (2013).
158. Karpiński, M., Jachura, M., Wright, L. J. & Smith, B. J. Bandwidth manipulation of quantum light by an electro-optic time lens. *Nat. Photonics* **11**, 53–57 (2017).
159. Lukens, J. M. et al. Generation of biphoton correlation trains through spectral filtering. *Opt. Express* **22**, 9585–9596 (2014).
160. Sośnicki, F., Mikołajczyk, M., Golestani, A. & Karpiński, M. Interface between picosecond and nanosecond quantum light pulses. *Nat. Photon.* **17**, 761–766 (2023).
161. Specht, H. P. et al. Phase shaping of single-photon wave packets. *Nat. Photon* **3**, 469–472 (2009).
162. Reimer, C. et al. High-dimensional one-way quantum processing implemented on d-level cluster states. *Nat. Phys.* **15**, 148–153 (2018).
163. Avenhaus, M., Eckstein, A., Mosley, P. J. & Silberhorn, C. Fiber-assisted single-photon spectrograph. *Opt. Lett.* **34**, 2873 (2009).
164. Davis, A. O. C., Thiel, V. & Smith, B. J. Measuring the quantum state of a photon pair entangled in frequency and time. *Optica* **7**, 1317 (2020).
165. Davis, A. O. C., Thiel, V., Karpiński, M. & Smith, B. J. Measuring the single-photon temporal-spectral wave function. *Phys. Rev. Lett.* **121**, 083602 (2018).
166. Davis, A. O. C., Saulnier, P. M., Karpiński, M. & Smith, B. J. Pulsed single-photon spectrometer by frequency-to-time mapping using chirped fiber Bragg gratings. *Opt. Express* **25**, 12804 (2017).
167. Gerrits, T. et al. Generation of degenerate, factorizable, pulsed squeezed light at telecom wavelengths. *Opt. Express* **19**, 24434 (2011).
168. Mittal, S. et al. Temporal and spectral manipulations of correlated photons using a time lens. *Phys. Rev. A* **96**, 043807 (2017).
169. Crockett, B. et al. Summing photon arrival times for dispersion-resilient quantum communications. In *2024 IEEE Photonics Conference (IPC)* (IEEE, 2024).
170. Grice, W. P. & Walmsley, I. A. Spectral information and distinguishability in type-II down-conversion with a broadband pump. *Phys. Rev. A* **56**, 1627–1634 (1997).
171. Jin, R.-B., Saito, T. & Shimizu, R. Experimental demonstration of time-frequency duality of biphotons. *Phys. Rev. Appl.* **10**, 034011 (2018).
172. MacLean, J.-P. W., Donohue, J. M. & Resch, K. J. Direct characterization of ultrafast energy-time entangled photon pairs. *Phys. Rev. Lett.* **120**, 053601 (2018).
173. Crockett, B., van Howe, J., Montaut, N., Morandotti, R. & Azaña, J. High-resolution time-correlated single-photon counting using electro-optic sampling. *Laser Photonics Rev.* **16**, 2100635 (2022).
174. MacLean, J.-P. W., Schwarz, S. & Resch, K. J. Reconstructing ultrafast energy-time-entangled two-photon pulses. *Phys. Rev. A* **100**, 033834 (2019).
175. U'Ren, A. B. et al. Generation of pure-state single-photon wavepackets by conditional preparation based on spontaneous parametric downconversion. *Laser Phys.* **15**, 146–161 (2005).
176. Javid, U. A. et al. Ultrabroadband entangled photons on a nanophotonic chip. *Phys. Rev. Lett.* **127**, 183601 (2021).
177. Kolchin, P., Belthangady, C., Du, S., Yin, G. Y. & Harris, S. E. Electro-optic modulation of single photons. *Phys. Rev. Lett.* **101**, 103601 (2008).
178. Harris, S. E. Nonlocal modulation of entangled photons. *Phys. Rev. A* **78**, 021807(R) (2008).
179. Crockett, B. et al. Exploiting nonlocal correlations for dispersion-resilient quantum communications (under review).
180. Karpiński, M., Davis, A. O. C., Sośnicki, F., Thiel, V. & Smith, B. J. Control and measurement of quantum light pulses for quantum information science and technology. *Adv. Quantum Tech.* **4**, 2000150 (2021).
181. Lu, H.-H., Liscidini, M., Gaeta, A. L., Weiner, A. M. & Lukens, J. M. Frequency-bin photonic quantum information. *Optica* **10**, 1655 (2023).
182. Sader, L. et al. Single-photon level dispersive fourier transform: ultrasensitive characterization of noise-driven nonlinear dynamics. *ACS Photonics* **10**, 3915–3928 (2023).
183. Thekkadath, G. S., Bell, B. A., Patel, R. B., Kim, M. S. & Walmsley, I. A. Measuring the joint spectral mode of photon pairs using intensity interferometry. *Phys. Rev. Lett.* **128**, 023601 (2022).
184. Dorrer, C. & Kang, I. Simultaneous temporal characterization of telecommunication optical pulses and modulators by use of spectrograms. *Opt. Lett.* **27**, 1315 (2002).
185. Wright, L. J., Karpiński, M., Söller, C. & Smith, B. J. Spectral shearing of quantum light pulses by electro-optic phase modulation. *Phys. Rev. Lett.* **118**, 023601 (2017).



186. Donohue, J. M., Mastrovich, M. & Resch, K. J. Spectrally engineering photonic entanglement with a time lens. *Phys. Rev. Lett.* **117**, 243602 (2016).
187. Lavoie, J., Donohue, J. M., Wright, L. G., Fedrizzi, A. & Resch, K. J. Spectral compression of single photons. *Nat. Photonics* **7**, 363–366 (2013).
188. Kuzucu, O., Wong, F. N. C., Kurimura, S. & Tovstonog, S. Joint temporal density measurements for two-photon state characterization. *Phys. Rev. Lett.* **101**, 153602 (2008).
189. Pirandola, S., Laurenza, R., Ottaviani, C. & Banchi, L. Fundamental limits of repeaterless quantum communications. *Nat. Commun.* **8**, 15043 (2017).
190. Van Loock, P. et al. Extending quantum links: modules for fiber- and memory-based quantum repeaters. *Adv. Quantum Tech.* **3**, 1900141 (2020).
191. Hilaire, P., Castor, Y., Barnes, E., Economou, S. E. & Grosshans, F. Linear optical logical Bell state measurements with optimal loss-tolerance threshold. *PRX Quantum* **4**, 040322 (2023).
192. Ansari, V., Donohue, J. M., Brecht, B. & Silberhorn, C. Tailoring nonlinear processes for quantum optics with pulsed temporal-mode encodings. *Optica* **5**, 534 (2018).
193. Jin, R.-B. et al. Quantum optical synthesis in 2D time–frequency space. *APL Photonics* **6**, 086104 (2021).
194. Belogolovskii, D., Alic, N., Grieco, A. & Fainman, Y. Silicon-rich nitride refractive index as a degree of freedom to maximize nonlinear wave mixing in nanowaveguides. *Adv. Photonics Res.* **5**, 2400017 (2024).
195. Dong, P., Chen, Y.-K., Duan, G.-H. & Neilson, D. T. Silicon photonic devices and integrated circuits. *Nanophotonics* **3**, 215–228 (2014).
196. Gupta, R. K., Chandran, S. & Das, B. K. Wavelength-independent directional couplers for integrated silicon photonics. *J. Lightwave Technol.* **35**, 4916–4923 (2017).
197. Micromachines. Grating couplers on silicon photonics: design principles, emerging trends and practical issues. <https://www.mdpi.com/2072-666X/11/7/666>.
198. Chen, G. et al. High-speed photodetectors on silicon photonics platform for optical interconnect. *Laser Photonics Rev.* **16**, 2200117 (2022).
199. Li, G. et al. Improving CMOS-compatible Germanium photodetectors. *Opt. Express* **20**, 26345–26350 (2012).
200. Coherent Corp. 43 GHz Balanced Photodetector. <https://ii-vi.com/product/43-ghz-balanced-high-speed-photodetector/>.
201. Liang, D., Huang, X., Kurczveil, G., Fiorentino, M. & Beausoleil, R. G. Integrated finely tunable microring laser on silicon. *Nat. Photon* **10**, 719–722 (2016).
202. Komljenovic, T. et al. Heterogeneous silicon photonic integrated circuits. *J. Lightwave Technol.* **34**, 20–35 (2016).
203. Wei, W.-Q. et al. Monolithic integration of embedded III-V lasers on SOI. *Light Sci. Appl.* **12**, 84 (2023).
204. Rahim, A. et al. Taking silicon photonics modulators to a higher performance level: state-of-the-art and a review of new technologies. *Adv. Photonics* **3**, 024003 (2021).
205. Witzens, J. High-speed silicon photonics modulators. *Proc. IEEE* **106**, 2158–2182 (2018).
206. Reed, G. T., Mashanovich, G., Gardes, F. Y. & Thomson, D. J. Silicon optical modulators. *Nat. Photon* **4**, 518–526 (2010).
207. Siew, S. Y. et al. Review of silicon photonics technology and platform development. *J. Lightwave Technol.* **39**, 4374–4389 (2021).
208. Han, H., Wang, J., Wang, Z., Liu, C. & Xiang, B. Integrated barium titanate electro-optic modulators operating at CMOS-compatible voltage. *Appl. Opt.* **62**, 6053–6059 (2023).
209. Li, W. et al. Thin-film BTO-based MZMs for next-generation IMDD transceivers beyond 200 Gbps/λ. *J. Lightwave Technol.* **42**, 1143–1150 (2024).
210. Kohli, M. et al. Plasmonic ferroelectric modulator monolithically integrated on SiN for 216 Gb/s data transmission. *J. Lightwave Technol.* **41**, 3825–3831 (2023).
211. Feng, H. et al. Integrated lithium niobate microwave photonic processing engine. *Nature* **627**, 80–87 (2024).
212. Wang, C. et al. Integrated lithium niobate electro-optic modulators operating at CMOS-compatible voltages. *Nature* **562**, 101–104 (2018).
213. Yu, M. et al. Integrated femtosecond pulse generator on thin-film lithium niobate. *Nature* **612**, 252–258 (2022).
214. Sun, Y. et al. Large group delay in silicon-on-insulator chirped spiral Bragg grating waveguide. *IEEE Photonics J.* **13**, 1–5 (2021).
215. Marom, D. M. et al. Compact colorless tunable dispersion compensator with 1000-ps/nm tuning range for 40-Gb/s data rates. *J. Lightwave Technol.* **24**, 237 (2006).
216. Tan, D. T. H., Sun, P. C. & Fainman, Y. Monolithic nonlinear pulse compressor on a silicon chip. *Nat. Commun.* **1**, 116 (2010).
217. Tan, D. T. H., Ikeda, K., Saperstein, R. E., Slutsky, B. & Fainman, Y. Chip-scale dispersion engineering using chirped vertical gratings. *Opt. Lett.* **33**, 3013–3015 (2008).
218. Sinatkas, G., Christopoulos, T., Tsilipakos, O. & Kriezis, E. E. Electro-optic modulation in integrated photonics. *J. Appl. Phys.* **130**, 010901 (2021).
219. Rahim, A. et al. Finite impulse response filter using 4-port MMI couplers for residual dispersion compensation. *J. Lightwave Technol.* **30**, 990–996 (2012).
220. Applied Nanotools Inc. <https://www.appliednt.com/> (2018).
221. Liu, J. et al. High-yield, wafer-scale fabrication of ultralow-loss, dispersion-engineered silicon nitride photonic circuits. *Nat. Commun.* **12**, 2236 (2021).
222. Skaar, J., Wang, L. & Erdogan, T. On the synthesis of fiber Bragg gratings by layer peeling. *IEEE J. Quantum Electron.* **37**, 165–173 (2001).
223. Kaushal, S., Roberge, A., Kashyap, R. & Azaña, J. Group-velocity dispersion compensation over a 70.56-km fibre-optic telecom link using a cm-long in-fibre device. In *2022 IEEE Photonics Conference (IPC)* 1–2 (IEEE, 2022).

## Acknowledgements

All authors acknowledge research funding from NSERC and FRQNT. C.R. acknowledges the FRQNT doctoral scholarship, and the Fondation INRS for the Andrea-Rovere scholarship. B.C. acknowledges NSERC for a Post-graduate Scholarship-Doctoral (PGS D) and SPIE for the D.J. Lovell Scholarship. MF acknowledges scholarships from NSERC and Mitacs Globalink. All authors acknowledge Fonex for valuable discussions.

## Author contributions

The introduction and Chapter 2 were written by C.R. and J.A. with input from B.C., while figures 1–4 were made by A.S. and C.R. Chapter 3 was written by X.Z., G.L., B.C., C.R., and J.A. Chapter 4 was written by M.G., M.F., B.C., and J.A. Chapter 5 was written by J.A. and C.R. Chapter 6 was written by B.C. and J.V.H. Chapter 7 was written by H.S., S.K., and J.A. The abstract and discussions were written by C.R. and J.A. All chapters were compiled, rearranged, and revised by C.R. and J.A. with discussions from the other authors.

## Competing interests

The authors declare no competing interests.

## Additional information

**Correspondence** and requests for materials should be addressed to José Azaña.

**Reprints and permissions information** is available at <http://www.nature.com/reprints>



**Publisher's note** Springer Nature remains neutral with regard to jurisdictional claims in published maps and institutional affiliations.

**Open Access** This article is licensed under a Creative Commons Attribution-NonCommercial-NoDerivatives 4.0 International License, which permits any non-commercial use, sharing, distribution and reproduction in any medium or format, as long as you give appropriate credit to the original author(s) and the source, provide a link to the Creative Commons licence, and indicate if you modified the licensed material. You do not have permission under this licence to share adapted material derived from this article or parts of it. The images or other third party material in this article are included in the article's Creative Commons licence, unless indicated otherwise in a credit line to the material. If material is not included in the article's Creative Commons licence and your intended use is not permitted by statutory regulation or exceeds the permitted use, you will need to obtain permission directly from the copyright holder. To view a copy of this licence, visit <http://creativecommons.org/licenses/by-nc-nd/4.0/>.

© The Author(s) 2025